Prepared by: ALMASpace, Chalmers, Cologne
Ref. number: AS-AWARDS-TR12
Version: 2.0
Date: June 11, 2011

AWARDS

Advanced microWAve Radiometers in Deep space Stations

Technical Report 12

REVIEW OF ALGORITHMS, MODELS, TECHNOLOGY, AND EXPERIMENTAL TECHNIQUES RELEVANT FOR THE MORE MCS

ESTEC Contract No. **23127/10/NL/LvH**

ALMA*Space* S.r.l
Headquarters: Via del Poggio 227, Panighina di Bertinoro (FC), I-47032
Head Office: Corso della Repubblica 19, Forlì (FC), I-47100
Tel: +39 054325280 Fax: +39 05431990220, www.almaspace.com
ESABD code: 13442

CHALMERS

Universität zu Köln

THIS PAGE IS INTENTIONALLY LEFT IN BLANK

Document Signature Table				
	Name	**Function**	**Signature**	**Date**
Authors:	Paolo Tortora	Project Manager		
	Alberto Graziani	Project Engineer		
	Gunnar Elgered	Senior scientist		
	Per Jarlemark	Senior scientist		
	Susanne Crewell	Senior scientist		
	Ulrich Löhnert	Scientist		
	Thomas Rose	Consultant		
Release:	Damiano Accurso	Contracts Officer		
Approval:	Paolo Tortora	Project Manager		

Document Change Record			
Issue/Revision	**Date**	**DCN No.**	**Changed Pages/Paragraphs**
1.0	July 29, 2010	AS-AWARDS-TR12	Initial Version
1.1	September 30, 2010	AS-AWARDS-TR12	Adjusted minor editing issues Chapter 3, included detailed layout of the ATPROP MWR Chapter 4, completed the stability characterization procedure Chapter 5, inserted results and comments of the effects of the preliminary location and configuration of the MCS Chapter 6, completed the operational issues
2.0	June 11, 2011	AS-AWARDS-TR12	Adjusted minor editing issues Chapter 3, inserted a review of the Total Power MWR. Chapter 4, moved the review of the mathematical methods for statistical characterization to AS-AWARDS-TR11. Added Sections 4.2 and 4.3.

Distribution List		
Internal		
Name		**No. Copies**
ALMASpace Archive		1
Chalmers University of Technology Archive		1
University of Cologne Archive		1
External		
Company/Organisation	**Name**	**No. Copies**
ESA-ESTEC	Linda van Hilten	1
ESA-ESTEC	Antonio Martellucci	1

Table of Contents

List of Figures

List of Tables

1 INTRODUCTION

This Technical Note has been prepared as deliverable document within the project entitled:

"Advanced microWAve Radiometers in Deep space Stations"

The Technical Note is part of the output of WP1100, WP1200 and WP1300, as reported on the proposal Technical Volume [AD. 4].

1.1 Structure Of The Document

This document contains the following sections:

- Introduction, including acronyms
- Applicable and reference documentation
- A review of the state of the art of the MWRs: the difference between the total power and the Dicke switch architecture and the instruments available at ESA and the JPL AMC system
- Some mathematical techniques and procedures developed for the stability characterization.
- A review of the models and remote sensing techniques developed to estimate the atmospheric fluctuations
- Preliminary interface and operational issues of the MCS

1.2 Acronyms

Abbreviation	Meaning
A/C	Aircraft
AD	Applicable Document
AMC	Advanced Media Calibration
AS	ALMASpace S.r.l.
ASD	Allan Standard Deviation
ATPROP	Atmospheric Propagation and Profiling system
AV	Allan Variance
AWVR	Advanced Water Vapor Radiometer
BLUE	Best Linear Unbiased Estimator
BWG	Beam Waveguide
CEI	Connected Element Interferometry
CESAR	Cabauw Experimental Site for Atmospheric Research
DSA	Deep Space Antenna
DSN	Deep Space Network
DSS	Deep Space Station
EO	Earth Observation
ESA	European Space Agency
ESOC	European Space Operations Centre
ESTEC	European Space Research and Technology Centre
ESTRACK	European Space Tracking network

Abbreviation	Meaning
GEO	Geostationary Earth Orbit
GNSS	Global Navigation Satellite System
GPS	Global Positioning System
GWE	Gravity Wave Experiment
HATPRO	Humidity and Temperature Profiler
HEF	High Efficiency
HPBW	Half-Power Beamwidth
HW	Hardware
IF	Intermediate Frequency
ITT	Invitation To Tender
JPL	Jet Propulsion Laboratory
KNMI	Koninklijk Nederlands Meteorologisch Instituut / Royal Netherlands Meteorological Institute
LAN	Local Area Network
LEO	Low Earth Orbit
LIDAR	Light Detection and Ranging
LNA	Low Noise Amplifier
LO	Local Oscillator
LOS	Line of Sight
LWP	Liquid Water Path
MCS	Media Calibration System
MORE	Mercury Orbiter Radioscience Experiment
MST	Mesosphere-Startosphere-Troposphere
MTP	Microwave Temperature Profiler
MU	Middle and Upper atmosphere
MWR	MicroWave Radiometer
NASA	National Aeronautics and Space Administration
PD	Path Delay
PM	Project Manager
RADAR	Radio Detection and Ranging
RD	Reference Document
Req.	Requirement
RF	Radio Frequency
RPG	Radiometric Physics GmbH
RSE	Radio Science Experiment
S/C	Spacecraft
SASD	Simplified Allan Standard Deviation
SCE	Solar Conjunction Experiment
SCIDAR	SCIntillation Detection and Ranging
SM	Surface Meteorological
SOW	Statement of Work
SW	Software
TB	Brightness Temperature
TBC	To Be Confirmed
TL	Treuhaft – Lanyi model
TR	Technical Report
TSF	Temporal Structure Function

Abbreviation	Meaning
VHF	Very High Frequency
VLA	Very Large Array
VLBI	Very Long Baseline Interferometry
vs.	Versus
WGN	White Gaussian Noise
WNP	White Noise Procedure
WPD	Wet Path Delay
WVR	Water Vapor Radiometer
ZHD	Zenith Hydrostatic Delay
ZTD	Zenith Total Delay
ZWD	Zenith Wet Delay

Table 1.1: Acronyms

1.3 Definitions

Definition	Symbol	Meaning
Air Mass		It is the air above a selected area. In the zenith direction air mass is 1. The air mass at a given elevation angle is then the value of the so-called mapping function.
Integration Time	Δt	It is the interval over which radiometry observables are averaged to reduce background noise and increase the signal-to-noise ratio
Observation Time	τ	It is the interval over which Doppler tracking observables are averaged to reduce background noise and increase the signal-to-noise ratio
Radiometric Accuracy		It is the extent to which measured brightness temperature agrees with its true value using calibration procedures.
Radiometric Resolution		It is the smallest change of brightness temperature that can be detected by the radiometer above the instrumental noise. It is sometime called as radiometric precision

Table 1.2: Definitions

2 APPLICABLE AND REFERENCE DOCUMENTS

2.1 Applicable Documents

Ref.	Title
[AD. 1]	Invitation to Tender SoW: *AO/1-6128/09/NL/LvH - Design Study for Precision Microwave Radiometer* – 23rd June 2009
[AD. 2]	Clarification no. 1 to Invitation to Tender: *AO/1-6128/09/NL/LvH* – 29 June 2009
[AD. 3]	Clarification no. 2 to Invitation to Tender: *AO/1-6128/09/NL/LvH* – 28 July 2009
[AD. 4]	ALMASpace ASEP00309 AWARDS Technical Volume - Volume II
[AD. 5]	ALMASpace ASEP00309 AWARDS Management Proposal - Volume III
[AD. 6]	ALMASpace ASEP00309_NM – Negotiation Meeting Minutes of Meeting
[AD. 7]	AS-AWARDS-TR11 – Comparison Between MORE and GWE MCS Requirement
[AD. 8]	AS-AWARDS-TR13 – Preliminary Location and Configuration of the MCS for Modelling the Effect of Atmospheric Turbulence

Table 2.1: Applicable Documents

2.2 Reference Documents

Ref.	Title
[RD. 1]	Abbate S.F., et al. “The Cassini Gravitational Waves Experiment”, Proceedings of the SPIE Conference 4856 on “Astronomy Outside the EM Spectrum”, August 2002, WaikoloaHI, USA
[RD. 2]	Alappattu D. P., and P. K. Kunhikrishnan, “First observations of turbulence parameters in the troposphere over the Bay of Bengal and the Arabian Sea using radiosonde”, J. Geophys. Res., 115, D06105, doi:10.1029/2009JD012916, 2010
[RD. 3]	Allan D.W., “Statistics of Atomic Frequency Standard”, Proceedings of the IEEE, 54, (2), 221-231, 1966
[RD. 4]	Arenas A., and A. J. Chorin, “On the existence and scaling of structure functions in turbulence according to the data”, Proc. Natl. Acad. Sci. USA 103**,** (12) 4352–4355,doi:10.1073/pnas0600482103,2003
[RD. 5]	Armstrong J. A., L. Iess, P. Tortora, B. Bertotti, “Stochastic Gravitational Wave Background: Upper Limits in the 10-6 to 10-3 Hz Band”, The Astrophysical Journal, Vol. 599, pp. 806-813, 20 December 2003
[RD. 6]	Armstrong, J.W. and R.A. Sramek, “Observations of tropospheric phase scintillations at 5 GHz on vertical paths”, Radio Sci., 17 (6), 1579-1586, 1982
[RD. 7]	ATPROP Technical Implementation Final
[RD. 8]	Avila, R., and J. Vernin, “Turbulence profiles with generalized scidar at San Pedro Martir observatory and isoplanatism studies”, Publ. Astron. Soc. Pacific, 110, 1106-1116, 1998.
[RD. 9]	Avila, R., J. Vernin, and E. Masciadri, “Whole atmospheric-turbulence profiling with generalized scidar”, Appl. Opt., 36(30), 7898-7905, 1997.
[RD. 10]	Azouit, M., and J. Vernin, “Optical turbulence profiling with balloons relevant to astronomy and atmospheric physics”, Publ. Astron. Soc. Pacific, 117, 536-543, doi: 10.1086/429785, 2005.

Ref.	Title
[RD. 11]	Bertotti B., L. Iess and P. Tortora, "A test of general relativity using radio links with the Cassini spacecraft", Nature, vol. 425, pp. 374-376, 25 September 2003
[RD. 12]	Bou-Zeid, E. C. Meneveau, and M. B. Parlange, "Large-eddy simulation of neutral atmospheric boundary layer flow over heterogeneous surfaces: Blending height and effective surface roughness" Water Resour. Res., 40, doi:10.1029/2003WR002475, 2004
[RD. 13]	Bregni, S, "Clock Stability Characterization and Measurement in Telecommunications", IEEE Trans. Instr. Meas., 46,(6), 1284-1294, 1997.
[RD. 14]	Carilli, C.L., and M.A. Holdaway, "Tropospheric phase calibration in millimeter interferometry", Radio Sci., 34 (4), 817-840, 1999.
[RD. 15]	Chadwick, R. B., and K. P. Moran, "Long-term measurements of Cn2 in the boundary layer", Radio Sci., 15 (2), 355-361, doi:10.1029/RS015i002p00355, 1980.
[RD. 16]	Crewell, S., and U. Löhnert, 2007: Accuracy of boundary layer temperature profiles retrieved with multi-frequency, multi-angle microwave radiometry. IEEE Transactions on Geoscience and Remote Sensing, 45(7), 2195-2201, DOI10.1109/TGRS.2006.888434.
[RD. 17]	D'Auria, G., F. S. Marzano, and U. Merlo, "Model for estimating the refractive-index structure constant in clear-air intermittent turbulence", Applied Optics, 32, 2674-2680, 1993.
[RD. 18]	Dicke R.H., "The Measurement of Thermal Radiation at Microwave Frequencies" Rev. Sci. Instr. Vol. 17, pag. 268-275, 1946
[RD. 19]	Egner, S.D., "Multi-Conjugate Adaptive Optics for LINC-NIRVANA: Laboratory tests of a Ground-Layer Adaptive Optics System and Vertical Turbulence Measurements at Mt. Graham", PhD thesis, Max-Planck-Institute for Astronomy, University of Heidelberg, Germany, 2006.
[RD. 20]	Feingold, G., A. S. Frisch, B. Stevens, and W. R. Cotton, "On the relationship among cloud turbulence, droplet formation and drizzle as viewed by Doppler radar", microwave radiometer and lidar, J. Geophys. Res., 104(D18), 22,195-203, 1999.
[RD. 21]	Fukao, S., M. D. Yamanaka, N. Ao,W. K. Hocking, T. Sato, M. Yamamoto, T. Nakamura, T. Tsuda, and S. Kato, "Seasonal variability of vertical eddy diffusivity in the middle atmosphere: 1. Three-year observations by the middle and upper atmosphere radar", J. Geophys. Res., 99, 18,973-987, 1994.
[RD. 22]	Gradinarsky, L. P., "Sensing Atmospheric Water Vapor Using Radio Waves", PhD Thesis, Chalmers Univ. Technol., Sweden, 2002.
[RD. 23]	Han Y., and E. R. Westwater, "Analysis and improvement of tipping calibration for ground-based microwave radiometers", IEEE Trans. Geosci. Remote Sens., 38(3), pages 1260– 1276, 2000.
[RD. 24]	Herbstreit, J.W., and M.C. Thompson, "Measurements of the phase of radio waves received over transmission paths with electrical lengths varying as a result of atmospheric turbulence", Proc. IRE, 43(10), 1391-1401, 1955.
[RD. 25]	Houghton, J. T., "The Physics of Atmospheres", Cambridge University Press, Cambridge, UK, 1997.
[RD. 26]	Iess L., Asmar S., Tortora P., "MORE: An advanced tracking experiment for the exploration of Mercury with the mission BepiColombo", Acta Astronautica, Vol. 65, 2009, pp. 666–675, doi:10.1016/j.actaastro.2009.01.049
[RD. 27]	Jacobson, A.R. and R. Sramek, "A method for improved microwave-interferometer remote sensing of convective boundary layer turbulence using water vapor as a passive tracer", Radio Sci., 32 (5), 1851-1860, 1997.
[RD. 28]	Jarlemark, P., and G. Elgered, "Retrieval of atmospheric water vapour using a ground-based single-channel microwave radiometer", Int. J. Remote Sensing, 24(19), 1366-5901, 2003.
[RD. 29]	Jarlemark, P.O.J., and T.R. Emardson, "Strategies for Temporal and Spatial Extrapolation and Interpolation of Wet Path Delay", J. Geodesy, 72, 350-355, 1998.
[RD. 30]	Jarlemark, P.O.J., T.R. Emardson, and J.M. Johansson, "Wet delay variability calculated from radiometric measurements and its role in space geodetic parameter estimation", Radio Sci., 33(3), 719-730, 1998.
[RD. 31]	Kao, C.-Y. J., D. I. Cooper, J. M. Reisner, W. E. Eichinger, and M. Ghil, "Probing near-surface atmospheric turbulence with high-resolution lidar measurements and models", J. Geophys. Res., 107(D10), 4081, doi:10.1029/2001JD000746, 2002.

Ref.	Title
[RD. 32]	Kassianides, C.N., and I.E. Otung, "Dynamic model of tropospheric scintillation on Earth-space paths", IEEE Proc. Microwave Antennas Propagat., 150(2), 97-104, 2003.
[RD. 33]	Kay, S. M., "Fundamentals of Statistical Signal Processing: Estimation Theory", Prentice Hall, New Jersey, 1993.
[RD. 34]	Keihm S. J., A. Tanner and H. Rosenberger, "Measurements and Calibration of Tropospheric Delay at Goldstone from the Cassini Media Calibration System", IPN Progress Report 42-158, August 15, 2004
[RD. 35]	Keihm, S. J., "Water Vapor Radiometer Measurements of the Tropospheric Delay Fluctuations at Goldstone over a Full Year", TDA Progress Report ,42- 122,l-11 ,1995.
[RD. 36]	Lay, O. P., "The temporal power spectrum of atmospheric fluctuations due to water vapour", Astron. Astrophys. Suppl. Ser. 122, 535-545, 1997.
[RD. 37]	Lesieur, M. and J. Herring, "Diffusion of a passive scalar in two-dimensional turbulence", J. Fluid Mech., 161, 77-95, 1985.
[RD. 38]	Linfield, R.P., S.J. Keihm, L.P. Teitelbaum, S.J. Walter, M.J. Mahoney, R.N. Treuhaft, and L.J. Skjerve, "A test of water vapor radiometer-based troposphere calibration using very long baseline interferometry observations on a 21-km baseline", TDA Progress Report, 42-122, 1995
[RD. 39]	Lüdi and Magun, "Refractivity structure constant and length scales from mm-wave propagation in the stably stratified troposphere", J. Atmos. Sol. Terr. Phys., 67, 435-447, 2005.
[RD. 40]	MORE Team, "MORE Science Performance Report (SPR)", Issue 2, Rev. 1, 6 Feb. 2009
[RD. 41]	Nastrom, G. D., and F. D. Eaton, "Relationship between refractivity turbulence intensity from MST radar observations and synoptic-scale vorticity", Radio Sci., 44, RS6003, doi:10.1029/2008RS004104, 2009.
[RD. 42]	Nastrom, G. D., and F. D. Eaton, "Seasonal variability of turbulence parameters at 2 to 21 km from MST radar measurements at Vandenberg Air Force Base", California, J. Geophys. Res., 110, D19110, doi:10.1029/2005JD005782, 2005.
[RD. 43]	Nath, D., M. Venkat Ratnam, A. K. Patra, B. V. Krishna Murthy, and S. V. Bhaskar Rao, "Turbulence characteristics over tropical station Gadanki (13.5¡N, 79.2¡E) estimated using high-resolution GPS and radiosonde data", J. Geophys. Res., 115, D07102, doi:10.1029/2009JD012347, 2010.
[RD. 44]	Naudet C., Jacobs C., Keihm S., Lanyi G., Linfield R., Resch G., Riley L., Rosenberger H., Tanner A. "The Media Calibration System for Cassini Radio Science: part I", TMO Progress report 42-143, 15 November 2000
[RD. 45]	Niell, A. E., "Global mapping functions for the atmosphere delay at radio wavelengths", J. Geophys. Res., 100, 3227-3246, 1996.
[RD. 46]	Nilsson, T., and R. Haas, "Impact of atmospheric turbulence on geodetic very long baseline interferometry", J. Geophys. Res., 115, B03407, doi:10.1029/2009JB006579, 2010.
[RD. 47]	Nilsson, T., J. L. Davis, and E. M. Hill, "Using ground-based GPS to characterize atmospheric turbulence", Geophys. Res. Lett., 36, L16807, doi:10.1029/2009GL040090, 2009.
[RD. 48]	Nilsson, T., L. Gradinarsky, and G. Elgered, "Correlations between slant wet delays measured by microwave radiometry", IEEE Trans. Geosci. Remote Sens., 43 (5), 1028-1035, doi:10.1109/TGRS.2004.840659, 2005.
[RD. 49]	Nörenberg D., S. Crewell, U.Löhnert, Th. Rose, A. Martellucci "A Novel Ground-based Microwave Radiometer for High Precision Atmospheric Observations Between 10 and 90GHz", IEEE International Geoscience and Remote Sensing Symposium, Boston, Massachusetts, USA, 6-11 July, 2008
[RD. 50]	Oswald J., L. Riley, A. Hubbard, H. Rosenberger, A. Tanner, S. Keihm, C. Jacobs, G. Lanyi, and C. Naudet, "Relocation of Advanced Water Vapor Radiometer 1to Deep Space Station 55", IPN Progress Report 42-163, November 15, 2005
[RD. 51]	Otarola, A, E. R. Kursinski, D. Ward, and R. Frehlich, "On the structure-function constant of the wet component of atmospheric index of refraction", submitted to Radio Sci., preprint, 2009.
[RD. 52]	Otung, I.E., and A. Savvaris, "Estimating tropospheric scintillation intensity on earth-space propagation paths", Electronics Letters, 42, 381-382, 2006.
[RD. 53]	Otung, I.E., and B.G. Evans, "Short term distribution of amplitude scintillation on a satellite link", Electronics Letters, 31(16), 1328-1329, 1995.
[RD. 54]	Rao, D. N., P. Kishore, T. N. Rao, S. V. B. Rao, K. K. Reddy, M. Yarraiah, and M. Hareesh, "Studies on refractivity structure constant, eddy dissipation rate and momentum flux at a tropical latitude", Radio Sci., 32(4), 1375-1389, 1997.

Ref.	Title
[RD. 55]	Rao, D. N., T. N. Rao, M. Venkataratnam, S. Thulasiraman, S. V. B. Rao, P. Srinivasulu, P. B. Rao, “Diurnal and seasonal variability of turbulence parameters observed with Indian mesosphere-stratosphere-troposphere radar”, Radio Sci., 36(6), 1439-1457, 2001.
[RD. 56]	Resch G. M., M. C. Chavez, and N. I. Yamane “Description and Overview of an Instrument Designed to Measure Line-of-Sight Delay Due to Water Vapor”, The Telecommunications and Data Acquisition Progress Report 42-72 October-December 1982
[RD. 57]	Resch G.M., Clark J.E., Keihm S.J., Lanyi G., Naudet C., Riley L., Rosenberger H., Tanner A. “The Media Calibration System for Cassini Radio Science: part II”, TMO Progress report 42-145, 15 May 2001
[RD. 58]	Resch G.M., Keihm S.J., Lanyi G., Linfield R.P., Naudet C., Riley L., Rosenberger H., Tanner A. “The Media Calibration System for Cassini Radio Science: part III”, IPN Progress report 42-148, 15 February 2002
[RD. 59]	Resch G.M:, D.E. Hogg, and P.J. Napier, “Radiometric correction of atmospheric path length fluctuations in interferometric experiments”, 19 (1), 411-422, 1984.
[RD. 60]	Roadcap, J. R., and P. Tracy, “A preliminary comparison of daylit and night Cn2 profiles measured by thermosonde”, Radio Sci., 44, RS2011, doi:10.1029/2008RS003921, 2009.
[RD. 61]	Rocca, A., F. Roddier, and J. Vernin, “Detection of atmospheric turbulent layers by spatiotemporal and spatio-angular correlation measurements of stellar-light scintillation”, J. Optical Soc. America, 64(7), 1000-1004, 1974.
[RD. 62]	Rose T., S. Crewell, U. Löhnert, and C. Simmer, “A network suitable microwave radiometer for operational monitoring of the cloudy atmosphere” Atmos. Res., 75(3), pages 183-200, 2005 doi:10.1016/j.atmosres.2004.12.005.
[RD. 63]	Russchenberg H, et al. “CESAR: Cabauw Experimental Site for Atmospheric Remote Sensing”, Proceedings of the XXVIIth General Assembly of the International Union of Radio Science, 17-24 Aug. 2002
[RD. 64]	Schön, S., and F.K. Brunner, “A proposal for modelling physical correlations of GPS phase observations”, J. Geod., 82, 601-612, 2008.
[RD. 65]	Schön, S., and F.K. Brunner, “Atmospheric turbulence theory applied to GPS carrier-phase data”, J. Geod., 82, 47-57, 2008.
[RD. 66]	Singh, M.S.J., S. I. S. Hassan, M. F. Ain, K. Igarashi, K. Tanaka, and M. Iida, “Analysis of tropospheric scintillation intensity on Earth to space in Malaysia”, Am. J. Appl. Sci. 3 (9), 2029-2032, 2006.
[RD. 67]	Somieski A., B. Bürki, A. Geiger, H.-G. Kahle, E. C. Pavlis, H. Becker-Ross, S. Florek, and M. Okruss, “Tropospheric water vapor from solar spectrometry and comparison with Jason microwave radiometer measurements”, J. Geophys. Res., 111, D09104, doi:10.1029/2005JD005767, 2006.
[RD. 68]	Stevens, B, and D. H. Lenschow, “Observations, Experiments, and Large Eddy Simulation”, Bulletin of the American Meteorological Society, 82, (2), 289-294, 2001.
[RD. 69]	Tanner A. B., “Development of a high stability water vapor radiometer”, Radio Science, Vol. 33, n. 2, Pages 449-462 March-April 1998
[RD. 70]	Tanner A. B., Riley A. L. “Design and performance of a high-stability water vapor radiometer”, Radio Science, Vol. 38, No 3, 8050, doi:10.1029/2002RS002673, 2003
[RD. 71]	Tatarski V. I., “The Effects of the Turbulent Atmosphere on Wave Propagation”, translated for NOAA by Israel Program for Scientific Translations, Jerusalem, 1971
[RD. 72]	Thompson, M.C., “A radio-optical dispersometer for studies of atmospheric water vapour”, Remote Sens. Environment, 2, 37-40, 1971
[RD. 73]	Tortora P., Iess L., Bordi J. J., Ekelund J. E., Roth D. C., “ Precise Cassini navigation during solar conjunctions through multifrequency plasma calibration”, Journal of guidance, control and dynamics, Vol. 27, No. 2, March-April 2004
[RD. 74]	Treuhaft, R. N., and G. E. Lanyi, “The effect of the dynamic wet troposphere on radio interferometric measurements”, Radio Sci., 22 (2), 251–265, doi:10.1029/RS022i002p00251, 1987.
[RD. 75]	VanZandt, T. E., J. L. Green, K. S. Gage, and W. L. Clark, “Vertical profiles of refractivity turbulence structure constant: Comparison of observations by the Sunset Radar with a new theoretical model”, Radio Sci., 13 (5), 819-829, doi:10.1029/RS013i005p00819, 1978
[RD. 76]	Vasseur, H., “Prediction of tropospheric scintillation on satellite links from radiosonde data”, IEEE Trans. Ant. Propagat., 47(2), 293-301, 1999

Ref.	Title
[RD. 77]	Walter, S.J., and P.L. Bender, "The slant path atmospheric refraction calibrator: an instrument to measure the microwave propagation delays induced by atmospheric water vapour", IEEE Trans. Geosci. Remote Sens., 30(3), 462-471, 1992.
[RD. 78]	Water vapor Radiometer ATPROP – "Users Manual"
[RD. 79]	Water vapor Radiometer RESCOM – "Users Manual"
[RD. 80]	Wheelon A. D., "Electromagnetic scintillation—I. Geometrical optics". Cambridge University Press, Cambridge, 2001.
[RD. 81]	Zink, F., R. A. Vincent, E. Murphy, and O. Cote, "Comparison of radar and in situ measurements of atmospheric turbulence", J. Geophys. Res., 109, D11108, doi:10.1029/2003JD003991, 2004.

Table 2.2: Reference Documents

3 REVIEW OF THE DESIGN OF CURRENT GROUND BASED MICROWAVE RADIOMETERS

Since the most crucial equipment of the troposphere media calibration system (MCS) is the microwave radiometer (MWR), in this chapter a review of the state of the art of ground-based MWRs is presented. Two radiometer technologies have been considered: the total power radiometer and the Dicke switch radiometer [RD. 18].

As far as the Dicke switch technology is concerned two different MWRs are reviewed: the so-called Advanced Water Vapor Radiometer (AWVR) developed by NASA JPL and the so-called ATPROP (Atmospheric Propagation and Profiling system) developed by ESA. As will be further detailed the AWVR is the main component of the Advanced Media Calibration (AMC) system, developed in 1998, to support the Cassini Gravity Wave Experiment (GWE), performed during the cruise phase of the mission. On the other hand, the ATPROP MWR is an instrument developed in the framework of the ESA ARTES activity in 2008, to support Earth Observation (EO) and telecommunication missions.

A crucial parameter used to characterize the MWR technologies and performances is the so-called Allan Standard Deviation (ASD) [RD. 3]. This figure of merit has been already presented in [AD. 7].

3.1 Total Power Radiometer

The simplest form of a microwave radiometer is the total power radiometer, Figure 3.1, that measures the noise power P_n available at the antenna due to thermal emission of a black body of temperature T:

$$P_n = k \cdot T \cdot B \tag{3-1}$$

Where B is the radiometer bandwidth measured in Hertz and k is the Boltzmann's Constant (1.38 10^{-23} J K^{-1}). Typical values of MWR are a bandwidth of B=200 MHz and an atmospheric emission temperature of 50 K which lead to a noise power in the order of 10^{-13} W. Therefore the atmospheric signal needs to be amplified by several orders of magnitude. This is even more pronounced as small variations, ΔT of the atmospheric emission, mainly caused by water vapour variations, shall be resolved. The minimum detectable temperature difference ΔT_{min} of an ideal total-power radiometer with integration time Δt can be calculated by using the ideal radiometer equation:

$$\Delta T_{\min} = \frac{T_{sys}}{\sqrt{\Delta t \cdot B}} \tag{3-2}$$

Where T_{sys} is the system noise temperature, which describes the temperature equivalent to the total noise power from all sources to the input of the receiver. For an ideal receiver it can be written as:

$$T_{sys} = T_R + T_A \tag{3-3}$$

Where T_A is the atmosphere and cosmic background radiation and T_R is the receiver noise temperature. In general, T_R is much larger than T_A.

In order to detect small signals, often cooled receivers are used to reduce T_R, however, this involves a much more complex design compared to uncooled receivers. Another approach to enable the detection of small microwave signals uses the super-heterodyne principle: where the scene signal is down-converted to a lower frequency where signal processing is simpler. In a heterodyne receiver (Figure 3.1), the radio frequency (RF) is down-converted to an intermediate frequency (IF) by a mixer using a frequency stable local oscillator (LO). In principle two sidebands with $V_{RF} = V_{LO} \pm V_{IF}$ are converted to the IF.

Since sensitive low noise amplifiers (LNAs) are nowadays available for frequencies below 100 GHz, heterodyne techniques are mostly applied at higher frequencies.

For real applications, the radiometric accuracy defined as the difference between the observed T_A to the true one, and the radiometric resolution, defined as the smallest detectable change in T_A need to be specified. In this respect, we have to define the overall gain G of a radiometer that relates the observed noise power to the system noise temperature as:

$$P_n = G \cdot k \cdot T \cdot B \tag{3-4}$$

Moreover, G is not constant with time. Gain fluctuation ΔG and noise fluctuations are independent random processes and their variances add in quadrature:

$$\sigma_{TOT}^2 = \sigma_{noise}^2 \cdot \sigma_G^2 \tag{3-5}$$

The practical total-power radiometer equation is defined as:

$$\Delta T_{\min} \equiv \sigma_{TOT} \approx T_{sys} \sqrt{\frac{1}{\Delta t \cdot B} + \left(\frac{\Delta G}{G}\right)^2} \tag{3-6}$$

One way to minimize the effects of gain fluctuations is to make a differential measurement by comparing the atmospheric signal with a reference signal. Rapid switching between both targets is performed via a Dicke switch named after Robert Dicke, Figure 3.1. Because equal viewing time for the atmosphere and the reference target reduces the duty cycle to 50 %, the minimum detectable temperature increases by a factor of 2.

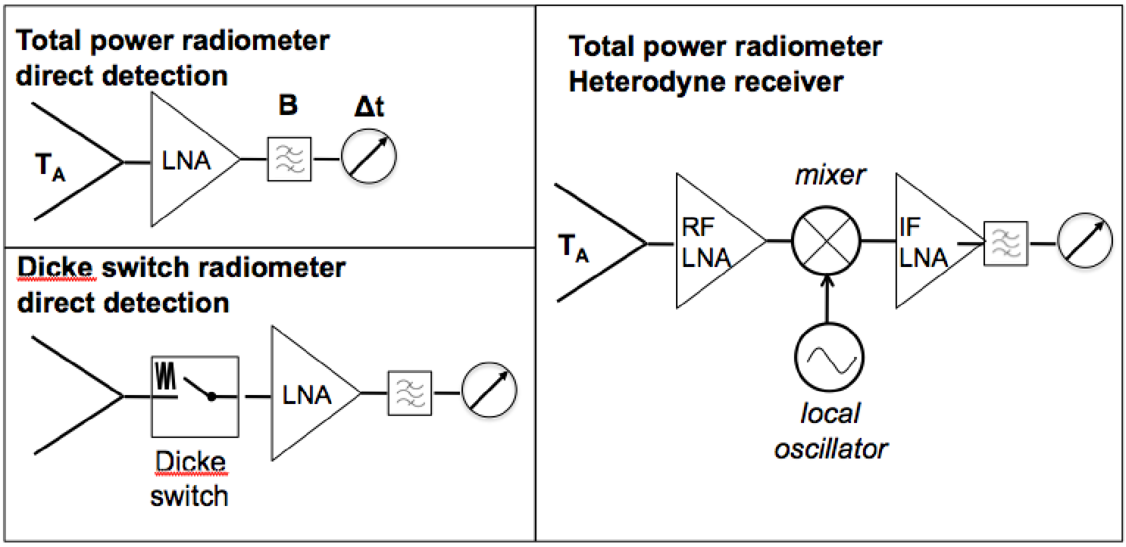

Figure 3.1: Sketch of different radiometer types. Low noise amplifiers (LNA) are implemented in the radio frequency (RF) and intermediate frequency (IF).

3.2 NASA Advanced Media Calibration System

In 2002 and 2003 a series of GWEs, aimed at the search for gravitational waves involving the Cassini S/C and the NASA DSN (Deep Space Network), were scheduled. In order to satisfy the radio link stability requirements for these experiments, JPL developed a newly ultra stable WVR in order to remove the troposphere path delay leaving an uncalibrated tropospheric noise in the Doppler observables characterized by an ASD of 1.5×10^{-15} s/s at 1000 s observation time.

For this reason, JPL developed two ultra stable Water Vapor Radiometers (WVR) [RD. 69], included in the so-called AMC system, where the main components of the system are: an ultra-stable WVR, a Surface Meteorological station (SM) with digital pressure sensors and a Microwave Temperature Profiler (MTP). The unit allows very precise measurements of the meteorological parameters like pressure and temperature and thanks to the WVR a very accurate measurement of the water vapor content along the line-of-sight (LOS) to the probe. For redundancy, JPL developed two AMC units.

The most critical aspect of the entire AMC system is the design of the WVR. Since the SM and the MTP are commercial equipments, the WVR has been entirely developed at JPL [RD. 69] [RD. 70]. Each WVR has an off-axis reflector giving a 1 deg beam width with very low side lobes. The azimuth and elevation pointing system offers a 0.1 deg pointing accuracy. The instrument is a three channel MWR which measures the brightness temperature at 22.2, 23.8 and 31.4 GHz. The 22.2 GHz channel close to the water vapor spectral line is used to measure the path delay, while the 23.8 and 31.4 GHz channels are used to reduce the sensitivity to variable height distribution of the water vapor and to detect the presence of clouds. Figure 3.2 shows one of the AMCS installed at the DSN complex of Madrid installed close to the DSS 55 (Deep Space Station). The AMC unit was relocated at the Madrid DSN complex in 2004 in order to increase the tracking capabilities during the Cassini Saturnian tour phase of the mission and for VLBI (Very Long Baseline Interferomerty) measurements [RD. 50].

Figure 3.2: NASA JPL AMCS unit installed at the DSN complex of Madrid close to the DSS 55

Studies to develop and deploy a MWR at the Goldstone DSN complex started in 70s to support radio astronomy observations as well as VLBI [RD. 56]. Since October 5, 1993 at NASA Goldstone DSN complex was installed a two channel R6 MWR, capable to measure brightness temperature at 20.7 and 31.4 GHz. The R6 MWR was operating in a continuous tip curve mode that provides calibration monitoring at clear weather conditions [RD. 35].

With the development of the Cassini mission to the Saturnian system, the characteristics of the R6 MWR were not able to satisfy the high demanding radio science experiments (RSE) requirements [RD. 1][RD. 5]. In particular, [RD. 35] reports the preliminary evaluation of the R6 performance compared with the Cassini GWE requirements. The evaluation is based on a one year of near-continuous WVR measurements collected at DSS 13 in Goldstone (CA). The collected data were processed in order to provide a statistical characterization of the Goldstone site in terms of ASD.

A comparison of the collected data with the previous Goldstone model results 30 to 35 % lower for long time scales up to 30 minutes. Seasonal variations have been detected in the order of 30-40 % from the annual mean ASD at all time scales. Summer months (June through September) with higher variations and winter months (November through March) with lower variations. Day/night variations have been detected in summer months, in particular during night time lowest values have been collected. On the other hands, during winter months not significant variations have been detected.

The comparison of the collected data with the GWE requirements reveals that the selected MWR performance is not capable to reach the GWE goals and requirements as shown in Figure 3.3.

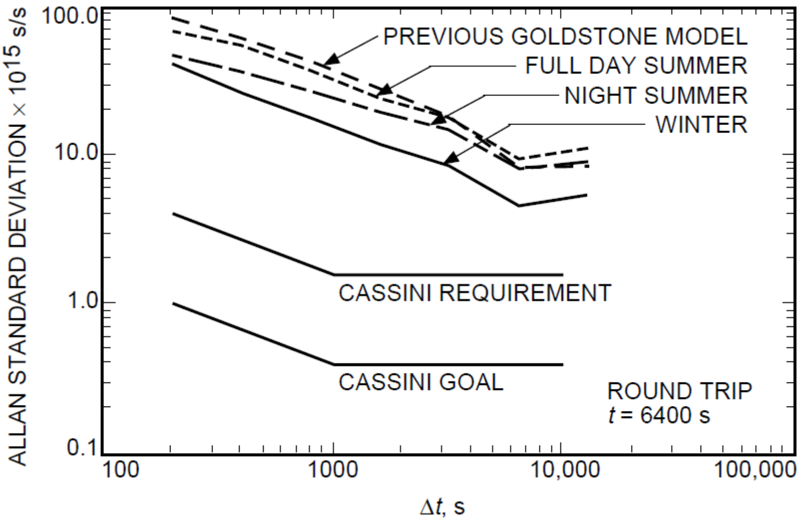

Figure 3.3: Comparison of modelled and WVR-measurements two-way ASD for Goldstone at 20-deg elevation with Cassini requirements and goals [RD. 35]

The Cassini requirements results about a factor of 10 greater than the MWR performance for time scales between 200 to 1000 s and a factor of 4 greater for time scales of 10000 s. Moreover, to met the Cassini goals the MWR performance should be scaled by a factor of 4 with respect to the Cassini requirements.

With the obtained results, a new troposphere calibration system should be developed with the capability to remove up to 90-98 percent of the troposphere fluctuations at all time scales. Even if at high observation time the calibration demand is less severe, it results that a system with greater stability at all observation times should be developed.

Starting from the previous results a preliminary WVR has been developed at JPL [RD. 69]. Important and critical aspects are presented in the first prototype: the temperature control system, the noise diode stability and a new design of the Dicke switch. Figure 3.4 shows the preliminary layout of the AWVR.

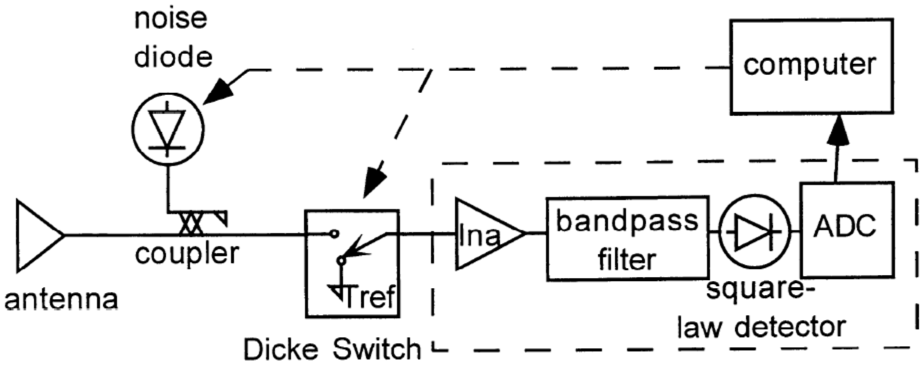

Figure 3.4: Layout of the AWVR [RD. 69]

Thanks to the results obtained during the laboratory test phase, the MWR presented standing waves which drove the design of a different configuration where two directional couplers were used to inject the noise diodes into a common waveguide path. Further tests revealed the two noise diode mismatch and the need to install a third noise diode capable to identify any single failure.

The final version of the AWVR is represented in Figure 3.5, where the temperature control and management system is represented, including the circulating air scheme.

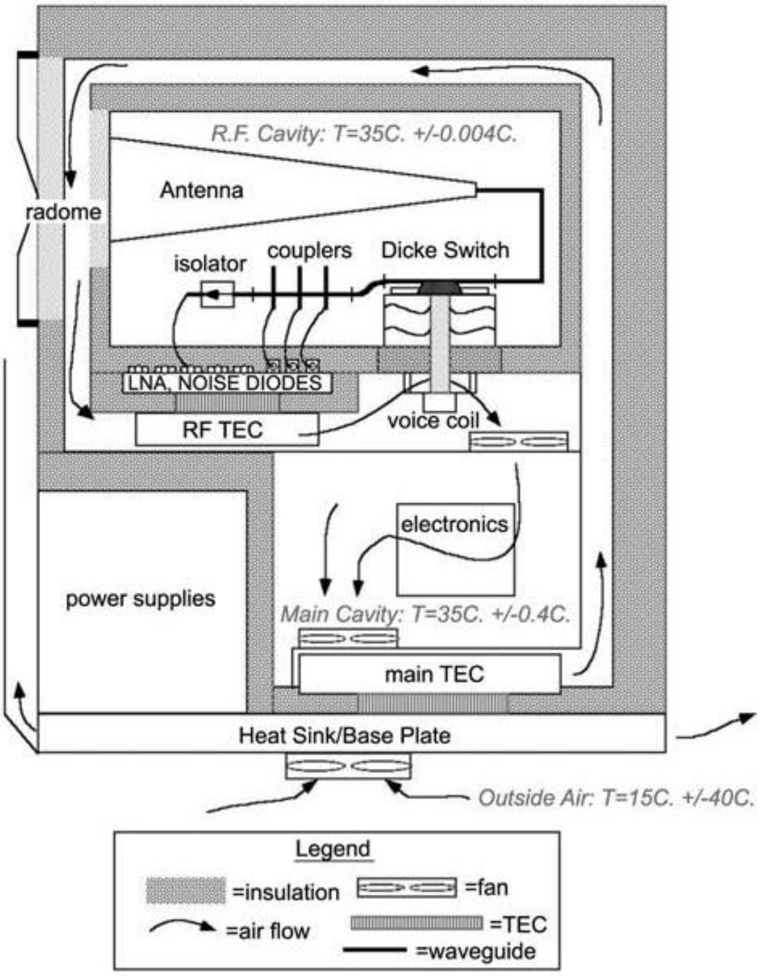

Figure 3.5: Cross section of the AWVR [RD. 70]

Laboratory experiments and performance evaluation have been undertaken: comparing the two radiometers and the tip curve calibration measured for more than a year.

The first performance estimation was the so-called "delta-T" were the short term of the two MWR was compared. In this activity both MWRs were pointed at Zenith and operated side-by-side in order to estimate the white noise. What was expected is that if the two MWR were perfectly stable and calibrated the result was the root-sum-square of the intrinsic noise of two MWRs. The result confirmed the good estimation of the radiometric stability requirement of 0.01 K at 1000s observation time. The measured stability was between 0.005 and 0.008 K at 1000 s.

In addition, the long-term stability of each AWVRs could be independently estimated form tip curve data over one year of collected data. This comparison showed that both instruments presented a small drift and only the 31.4 GHz channel presented significant long term errors. However, the result of the tip-curve calibration was an estimation of a one-month stability of about 0.05 K. The AMCS met the GWE stability requirements. In particular at time scales of 1000 to 10000 s the stability goal of 0.01 K was obtained, with some channels approaching in some cases a value of 0.003 K [RD. 70].

The data analysis revealed some problems and the Cassini requirements were met only in some cases. This behaviour was attributed to systematic errors in the interferometric system [RD. 57].

Figure 3.6 shows the ASD of the WPD (Wet Path Delay) at the DSS 25 during the main Cassini experiment: GWE and the SCE (Solar Conjunction Experiment).

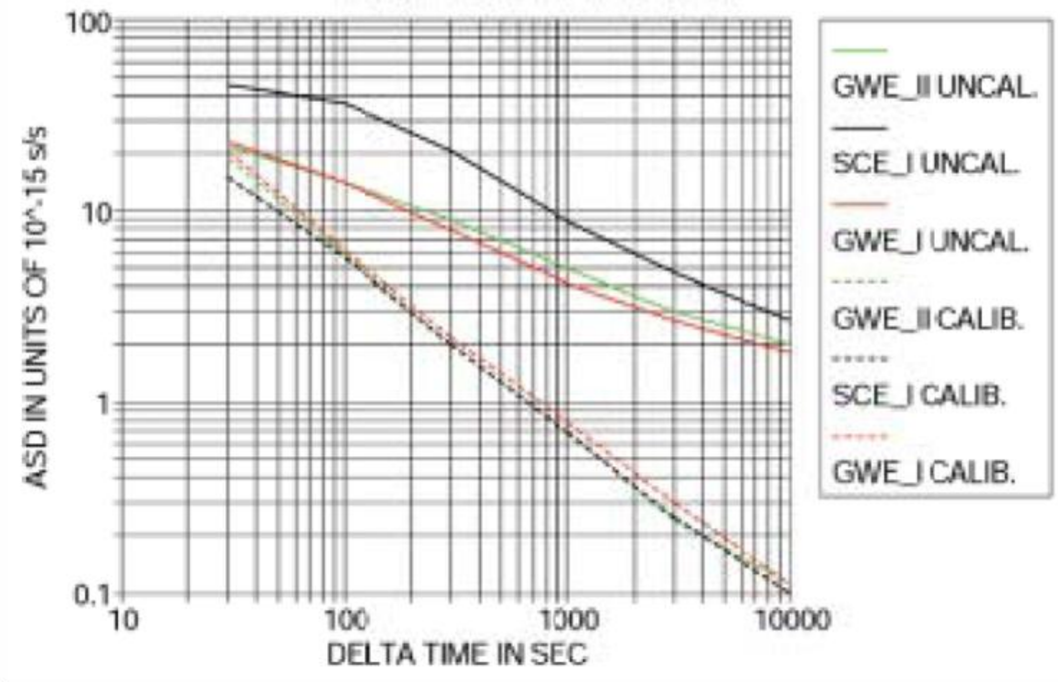

Figure 3.6: ASD of the WPD at the DSS 25 during three CAssini radio science experiments [RD. 34]

3.2.1 Comparison Experiment: MCS vs CEI

A further test campaign was carried out in late 1999 and early 2000 in order to study the AMC system performance. Two AMC units were placed close a corresponding DSN antenna of the VLBI network, in order to compare two independent measure of the troposphere path delay fluctuations.

On [RD. 44] [RD. 57] [RD. 58] the experiment is fully described, presenting strategies, data analysis procedure, weather conditions error budget and performance evaluation.

In this paragraph, the experiment is described and the main results are reported.

The experiment layout is shown in Figure 3.7. In principle, the interferometer is sensitive to any difference in the path delay of the two interferometer elements. The VLBI observable is the phase-delay difference between the signals arriving at each station. Modelling and subtracting each geometric effect from the VLBI observables, it results that the residual phase is dominated by the unmodelled effects: the water vapour fluctuations.

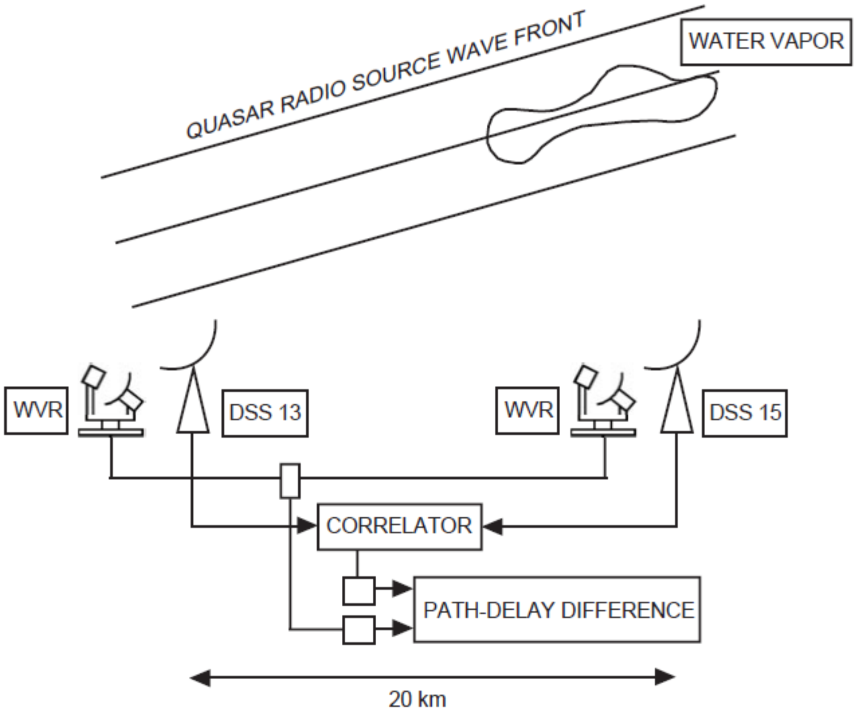

Figure 3.7: Schematic illustration of the comparison experiment carried out between the AMC system and the radio interferometer [RD. 44]

The VLBI stations selected were the 34 m diameter beam wave guide (BWG) antenna DSS 13 and the 34 m diameter high efficiency (HEF) antenna DSS 15 linked in a Connected Element Interferometer (CEI) configuration. The CEI experiment collected a series of dual-frequency (2.3 GHZ and 8.4 GHz) observations pointing to a well-known quasar position.

Each AMC unit was located at a distance of about 50 m with respect to the DSS. Since AMC and DSS were co-pointed the distance position was selected in order to maximize the sky coverage while minimizing the beam offset errors.

A crucial aspect of this experiment was that considering the length of the baseline (about 20 km) with an average wind speed below 5-10 m/s, the troposphere path delay fluctuations result independent for timescales below 4000 s.

As already mentioned the experiments were carried out as follow. CEI data acquired at each DSS antenna were cross–correlated and the interferometric time delay was extracted. The measured time delay was subtracted from an a priori model in order to obtain the residual phase delay and delay rate. The residual data includes a differential clock-like term which was removed by statistical estimation, including the linear term of the troposphere path delay.

On the other hand, the AMC data were collected during each quasar tracking and processed in order to have a derived path delay time series. The AMC path delay was smoothed at 6 s integration time and the data from each site were subtracted each other to create a site differenced time series. Finally, the linear part of the differential delay was removed and the resulted time series could be compared with the CEI residuals. For ease of comparison both CEI and AMC data sets were mapped in the zenith direction and the Zenith Path Delay (ZPD) was compared. Figure 3.8 shows the residual ZPD measured from CEI and differenced AMC.

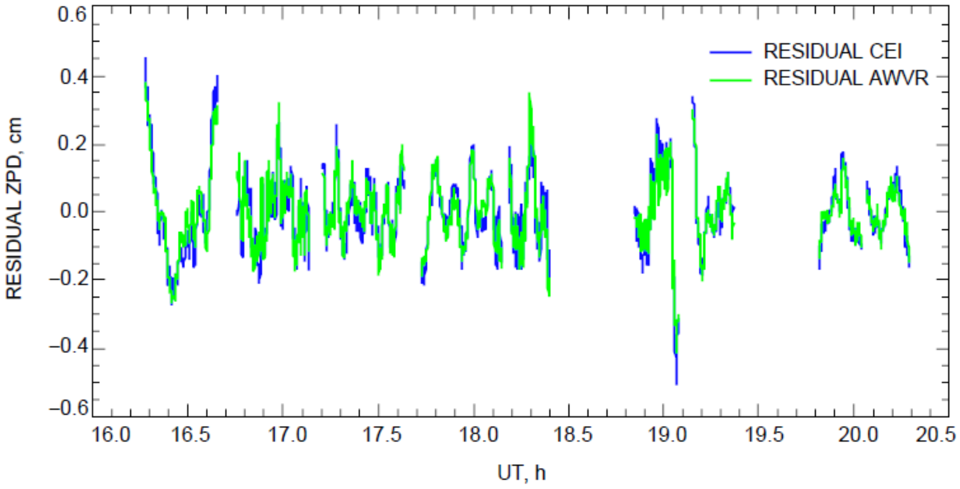

Figure 3.8: Residual ZPD measured from CEI (blue) and differenced AMC (green) after the linear trend is removed from each [RD. 57]

In order to better evaluate the AMC performance, estimated CEI fluctuations were calibrated with AMC data by subtracting each other data, Figure 3.9.

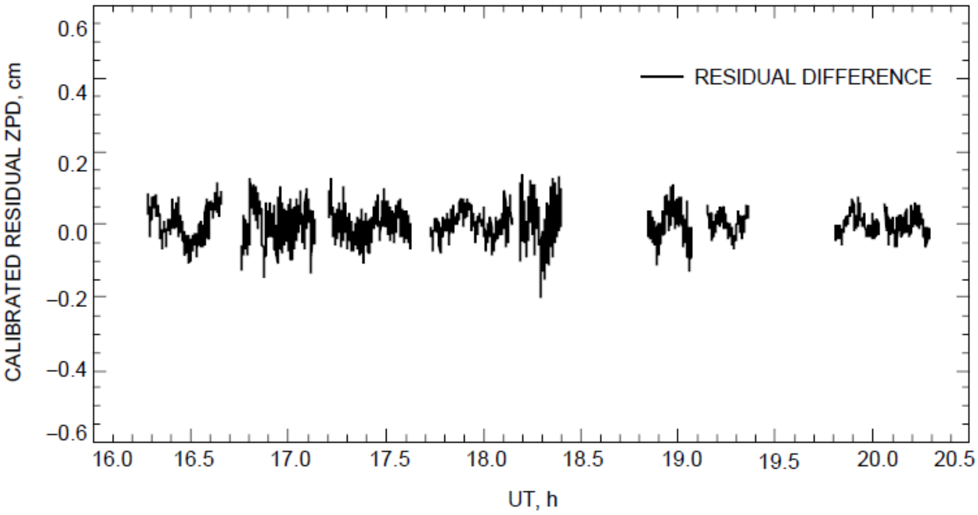

Figure 3.9: Residual CEI path delay after AMC calibration [RD. 57]

For each experiment, the time series were limited to a duration of about 26 min, but due to instrumental, operational and weather troubles the data available for the analysis was partial.

A representative experiment was carried out on DOY 240, 1999, where 11 scans were collected. For each scan the ASD was computed and compared with the Cassini requirement. Figure 3.10 shows the worst performance scan (a) and the best performance scan (b), where the WVR data, the calibrated and uncalibrated CEI data are reported. A significant result was obtained with the best performance by calibrating the CEI measurements. It results that the Cassini requirement was satisfied for observation time up to 200-300 s.

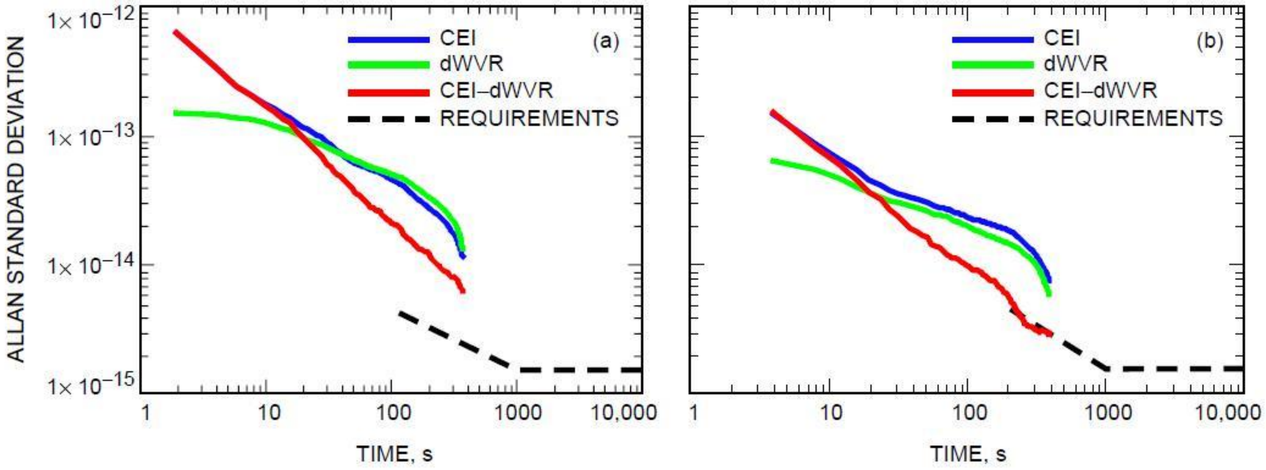

Figure 3.10: ASD plotted as function of time for DOY 240,1999. (a) scan 7, worst performance. (b) scan 11, best performance [RD. 57]

Long time comparing were not available due to instrumental trouble in DSS 13 up to May 2000. Once the problem was corrected a series of long time experiment was carried out. On DOY 137, 2000 and 138, 2000.

The ASD of the experiment on DOY 138,2000 is plotted in Figure 3.11, where the WVR data, the uncalibrated and the calibrated CEI data are reported. It results that the Cassini requirements are satisfied for observation time above 2000 s. At the same time, below 1000 s observation time the MCS performance fails to satisfy the requirement by a factor of 2-3.

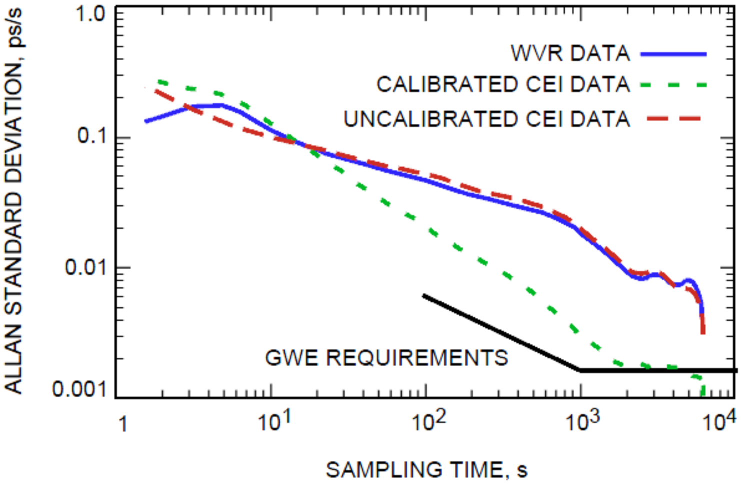

Figure 3.11: ASD plotted as a function of sampling time for the long scan of DOY 138, 2000 [RD. 44]

This result was probably a combination of different effects: unknown CEI errors and the AMC-CEI 50 m offset.

In conclusion the AMC system is capable to reduce the uncalibrated stability of CEI by a factor of 2-3 in the range of 100-1000 s observation time. The entire experiment results show that the AMC are capable to reduce the path delay at 1 mm level in semidry conditions. For this reason, the use of AMC to calibrate tracking data allows a reduction of the error in the S/C orbit determination.

3.3 ESA/ESTEC Microwave Radiometers for Telecom

Two ESA MWRs are installed at the atmospheric remote sensing station of Cabauw, The Netherlands, of the KNMI, in the framework of the National Dutch CESAR project [RD. 63].

The instrument technologies are very diverse and have been developed in different time slots. An important issue is that both instruments are developed with the Dicke switch technology.

3.3.1 RESCOM Microwave Radiometer

The first instrument is the RESCOM A/S 20/30 GHz radiometer [RD. 79], developed in the early 90s for geostationary satellite navigation and meteorological missions, Figure 3.12. The instrument is a 3 channels MWR at 21.3 23.8 and 31.4 GHz with a very simple and efficient architecture and a temperature monitoring system.

Figure 3.12: The RESCOM MWR installed at Cabauw remote sensing site

The main characteristic is the division of the RF system (front-end and PCB) in two separated lines: one for the water vapour channels (21.3 GHz and 23.8 GHz) and the other for the liquid water channel (31.4 GHz).

Table 3.1 summarizes the main characteristics of the RESCOM MWR. In particular, the instrument radiometric resolutions are computed at two different integration time: 1s and 4 s [AD. 7]. The pointing uncertainty reported is referred to the only elevation, since the current version of the MWR has the only elevation rotator.

Channel [GHz]	Bandwidth [MHz]	Radiometric Resolution @ 1s [K]	Radiometric Resolution @ 4s [K]	Pointing Uncertainty (El) [deg]
21.30	2x40	0.3	0.07	0.5
23.80	2x40	0.3	0.07	0.5
31.40	2x40	0.3	0.07	0.5

Table 3.1: Resume of the RESCOM MWR main characteristics

The instrument layout is shown in Figure 3.13 which highlights the two RF lines. Both lines are equal, with the same components and the same architecture. Both RF lines share a common feed horn and antenna dish.

A crucial characteristic of the RESCOM MWR is its thermal system. The RF system is housed in an insulated, temperature regulated box, designed to provide an internal temperature of 40°C ± 1° C with a range of external temperature between 20° C and 50 ° C.

The thermal system is based on a combination of sensors and Peltier-elements. The sensors are distributed in the RF system in order to monitor the temperature of the main components: red dots in Figure 3.13 represents the position of the temperature sensors. On the other hand, the Peltier-elements are the active component of the thermal system, which take care to heat or cool the RF system. The Peltier-elements are connected with the front-end mounting plates.

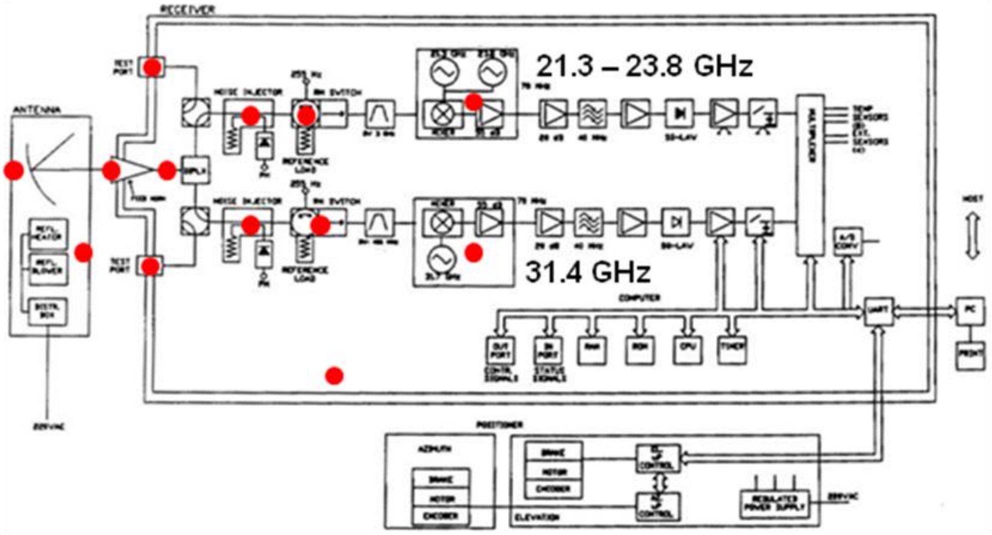

Figure 3.13: Layout of the RESCOM MWR, red dots indicates the position of the temperature sensors

Some aspects of the instrument prevent its use for radio science activities. As already mentioned, the RESCOM MWR has only an elevation rotor which it does not fit with the tracking requirements of a deep space mission. Moreover the MWR is remotely controlled by a computer based on an old software version.

On the other hand, the MWR is well tested and it has been used for ages collecting lots of data. The MWR and its database can be used for a comparison in a testing campaign of the performance of other instruments.

3.3.2 ATPROP Microwave Radiometer

The last ESA MWR developed is the RPG ATPROP Ka-band radiometer [RD. 49]. This instrument was developed by RPG in 2008 in collaboration with the University of Cologne in the framework of ARTES [RD. 78] [RD. 7]. Figure 3.14 shows the ATPROP MWR installed in Cabauw (NL).

Different purposes drove the development of this MWR. Its major purposes was to support all satellite missions orbiting the Earth: from LEO to GEO, in particular, for telecommunication and EO missions calibration.

Figure 3.14: The ATPROP MWR installed at Cabauw remote sensing site

In principle the ATPROP has been designed to investigate the atmosphere attenuation in a wide frequency range: from 15 GHz to 90 GHZ. For this reason the instrument is based on a combination of the RPG HATPRO (Humidity and Temperature Profiler) [RD. 62] and a dedicated radiometer designed to investigate only the 15 GHz and 90 GHz channels, named R15-90. While HATPRO is a total power radiometer (see Figure 3.1) the Ka-band channels of ATPROP employ a combination of Dicke and noise diode switching, Figure 3.16.

The ATPROP MWR presents fourteen channels: six in the water vapour line (22.24 – 27.84 GHz), one in the liquid water line (31.4 GHz), seven in the oxygen line for temperature profiling (51.24 – 58.00 GHz) plus the already mentioned 15.3 GHz for precipitations and 90 GHz channel for improvement LWP retrievals.

Each channel presents different characteristics in terms of rms noise level, beamwidth and Half Power Beamwidth (HPBW) and a common pointing precision level as reported in Table 3.2.

As far as the pointing system is concerned, the MWR is installed in a dedicated azimuth rotator, capable to move in the entire 360 deg. On the other hand each subsystem (HATPRO and R15-90) includes a dedicated elevation rotator which moves their antenna. Thanks to this combination, the ATPROP is capable to scan completely the sky.

Channel [GHz]	Bandwidth [MHz]	HPBW [deg]	Elevation Accuracy [deg]	Azimuth Accuracy [deg]	Rms Noise [K]
15.30	200	6.2	0.3	0.1	0.15
22.24	230	3.9	0.3	0.1	0.1
23.04	230	3.8	0.3	0.1	0.1
23.84	230	3.6	0.3	0.1	0.1
25.44	230	3.4	0.3	0.1	0.1
26.24	230	3.4	0.3	0.1	0.1
27.84	230	3.3	0.3	0.1	0.1
31.40	230	3.2	0.3	0.1	0.1
51.26	230	2.0	0.3	0.1	0.2
52.28	230	2.0	0.3	0.1	0.2
53.86	230	1.9	0.3	0.1	0.2
54.94	230	1.9	0.3	0.1	0.2
56.66	600	1.8	0.3	0.1	0.2
57.30	1000	1.7	0.3	0.1	0.2
58.00	2000	1.7	0.3	0.1	0.2
90.00	2000	3.0	0.3	0.1	0.2

Table 3.2: Characteristics of the ATPROP channels in terms of beamwidth, HPBW, pointing accuracy and rms noise level

Figure 3.15 shows the distribution of the ATPROP channels (HATPRO and R15-90) in the atmosphere absorption spectrum.

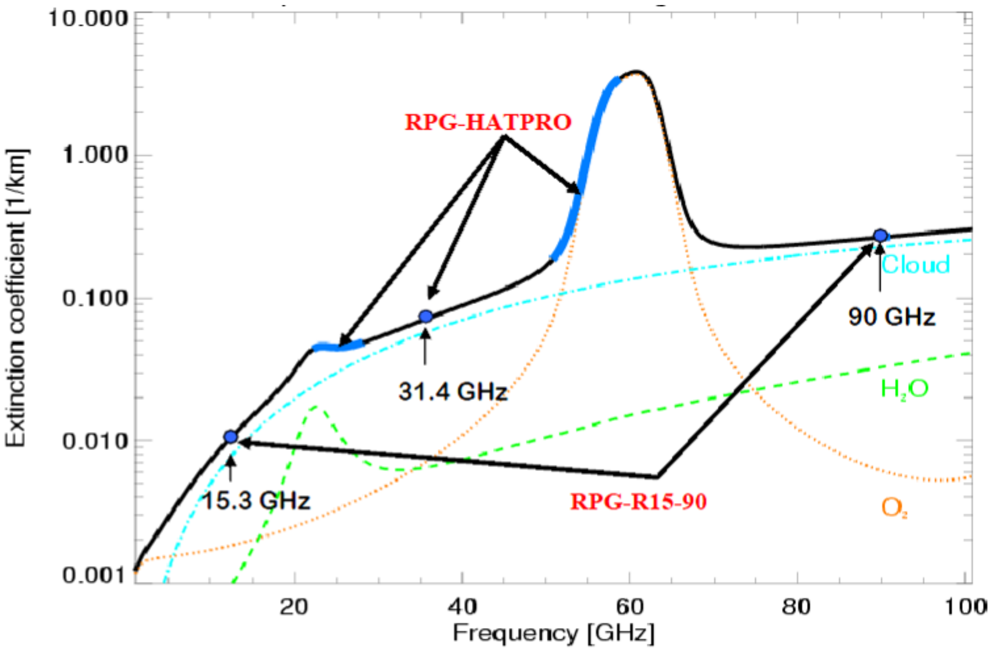

Figure 3.15: Distribution of the ATPROP channels in the atmosphere spectrum [RD. 7]

The internal architecture of the ATPROP is completely different, compared with the RESCOM one presented in Figure 3.13. The layout presented in Figure 3.16 shows the presence of a common RF line of the instrument where all the channels are connected in parallel. This architecture is named filter bank concept. In this architecture, besides the antenna, all the channels shares the Dicke switch, the noise diode and the LNA.

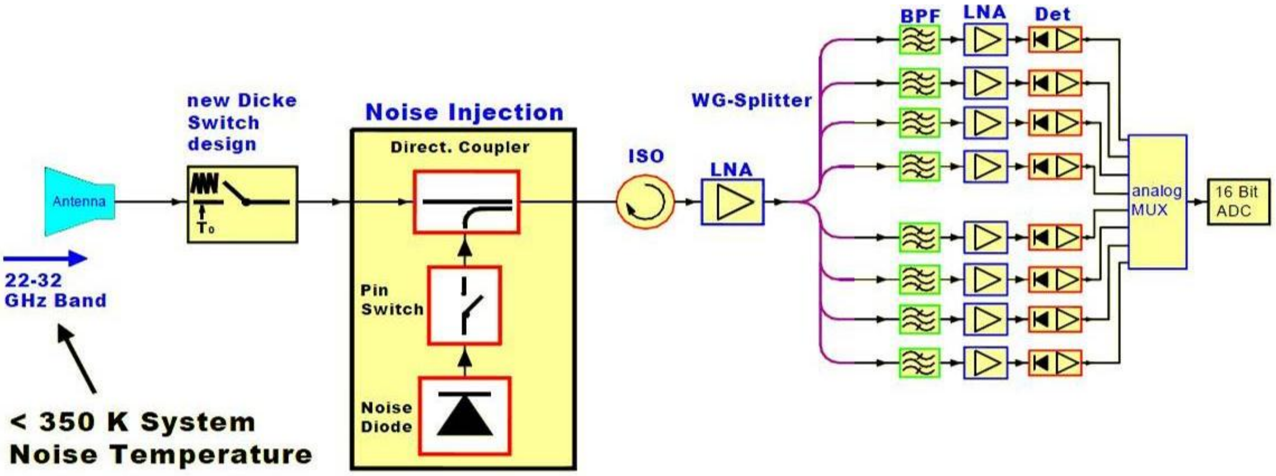

Figure 3.16: Layout of the HATPRO side of the ATPROP MWR [RD. 7]

The development of this architecture presents some advantages compared to an heterodyne system:

- Stability improvement: thanks to limits in the frequency and amplitude drifts of the local oscillators
- Cost reduction: mixers and sideband filtering are not requested
- Reduced sensitivity to interfering due to avoidance of frequency down conversion

Moreover the filter bank concept presents some improvements and advantages:

- Simultaneous measurement of all the frequency channels
- Faster calibration procedure, a single calibration is sufficient for all the channels
- Individual channel bandwidth selection, which allows the definition o the boundary layer temperature profiler [RD. 16].

During the development phase, the ATPROP has been characterized in terms of ASD at different observation time (1 s, 10 s, 100 s and 1000 s) pointing the instrument to a stable laboratory cold load. Table 3.3 reports the results of the characterization indoor campaign.

Channel [GHz]	ASD @ 1s	ASD @ 10s	ASD @ 100s	ASD @ 1000s
22.24	0.151	0.053	0.0226	0.0099
23.04	0.150	0.055	0.0230	0.0098
23.84	0.144	0.044	0.0228	0.0100
25.44	0.169	0.052	0.0266	0.0107
26.24	0.180	0.053	0.0272	0.0099
27.84	0.177	0.052	0.0273	0.0111
31.40	0.215	0.070	0.0351	0.0157
51.26	0.222	0.073	0.0372	0.0161
52.28	0.227	0.078	0.0347	0.0163
53.86	0.233	0.078	0.0358	0.0203
54.94	0.259	0.082	0.0393	0.0154
56.66	0.196	0.067	0.0353	0.0155

Channel [GHz]	ASD @ 1s	ASD @ 10s	ASD @ 100s	ASD @ 1000s
57.30	0.177	0.060	0.0357	0.0137
58.00	0.178	0.063	0.0437	0.0158
15.30	0.250	0.085	0.0613	0.0273
90.00	0.244	0.083	0.0646	0.0366

Table 3.3: Allan Standard Deviation of the ATPROP channels at different observation time

A very crucial procedure of the ATPROP MWR is its calibration. The absolute calibration of ATPROP is done either manually using a 4-point calibration technique for all channels or for transparent frequency channels using an automatic tipping curve procedure [RD. 23]. The 4-point calibration is typically done when the radiometer has been transported or at intervals of several months. It involved reference loads at liquid nitrogen T_C, and ambient temperature T_H. In order to derive the non-linearity factor α, both reference targets are also viewed with an additional noise signal at T_N:

$$P_{CN/HN} = G\left(T_R + T_{C/H} + T_N\right)^{\alpha} \tag{3-7}$$

Note that, instead of physical temperature, the Planck equivalent is correctly implemented in the ATPROP software. With the 4-point calibration method also the noise diode equivalent temperature T_n is determined. Assuming a high radiometric stability of the noise injection temperature, following calibrations can use this secondary standard (together with the built-in ambient temperature target) to recalibrate T_{sys} and G (considering α to be constant).

The noise adding radiometer removes gain fluctuations, which are the major source of fluctuations and drifts. The noise calibration does not account for drifts in receiver noise temperature T_R. It turns out that gain drifts are by far the most critical calibration issue. T_R drifts are much slower (in the order of hours or days), in particular if the physical receiver temperature is accurately stabilized. In order to calibrate T_r drifts, the receivers continuously activate the Dicke switches, but only for 10% of the calibration cycle as presented in Figure 3.17. At least 100 calibrations are averaged before TR is re-adjusted. Therefore, the radiometer duty cycle is only reduced to 45%.

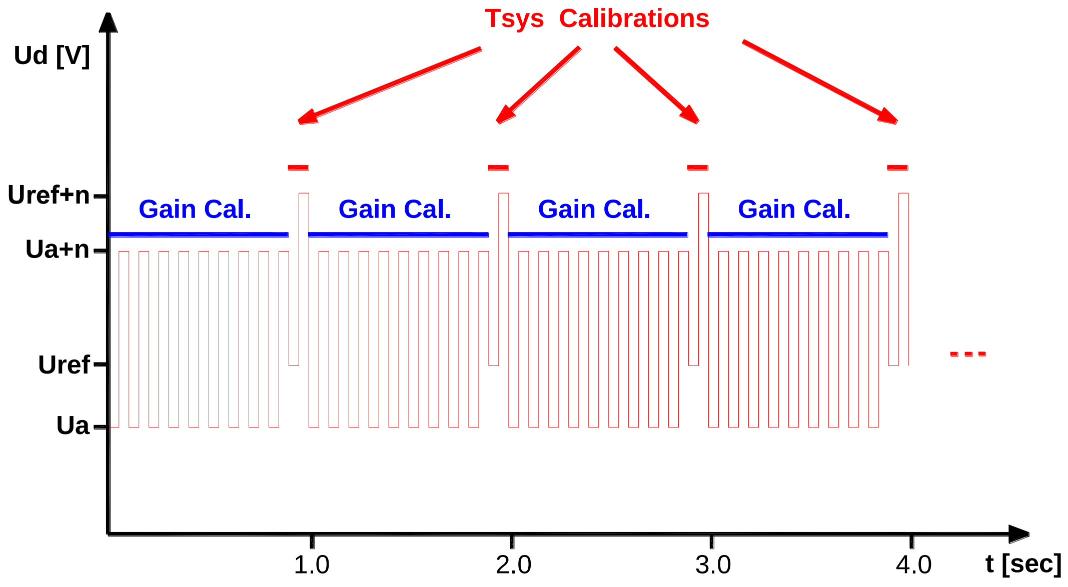

Figure 3.17: Calibration timing scheme. Noise adding is performed 10 times as often as Dicke switch activation

4 REVIEW OF TECHNIQUES FOR THE STABILITY CHARACTERIZATION OF MICROWAVE RADIOMETER

In this chapter will be presented different procedures for the characterization of the stability and the performance of the MWR. The analysis use the mathematical methods presented in [AD. 7], in particular the instruments will be characterized in terms of ASD.

4.1 Stability Characterization Procedure

In order to evaluate the performance requirements of the MCS, a precise procedure will include the use of both the ASD and the TSF (Temporal Structure Function). The proposed method is based on the procedure used in the past for the characterization of the NASA JPL AMCS [RD. 34].

As discussed in many studies the main problem of the interpretation of the ASD is that the obtained result is the sum of the stability of the instrument and the variations in the atmosphere. For this reason the different components to the ASD should be identified and accounted for separately.

A preliminary evaluation criteria for the separation of the two contribution is here proposed by considering the data collected with the ATPROP MWR in Cabauw (NL) on April 21st 2008. The time series of the analyzed Zenith Wet Delay (ZWD) is reported in Figure 4.1, while Figure 4.2 shows the brightness temperature (TB) at the water vapor channel 23.8 GHz.

The collected data for that day were selected as a free of liquid water day. In particular the retrieval of the ZWD was mainly related to the water vapor channel.

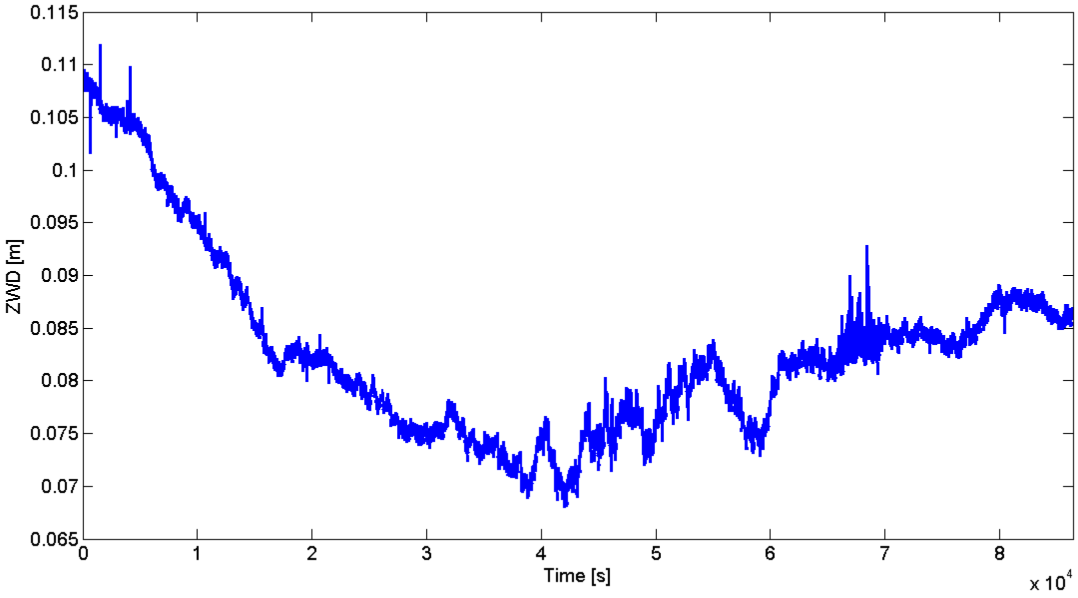

Figure 4.1: Retrieved ZWD of the ATPROP MWR

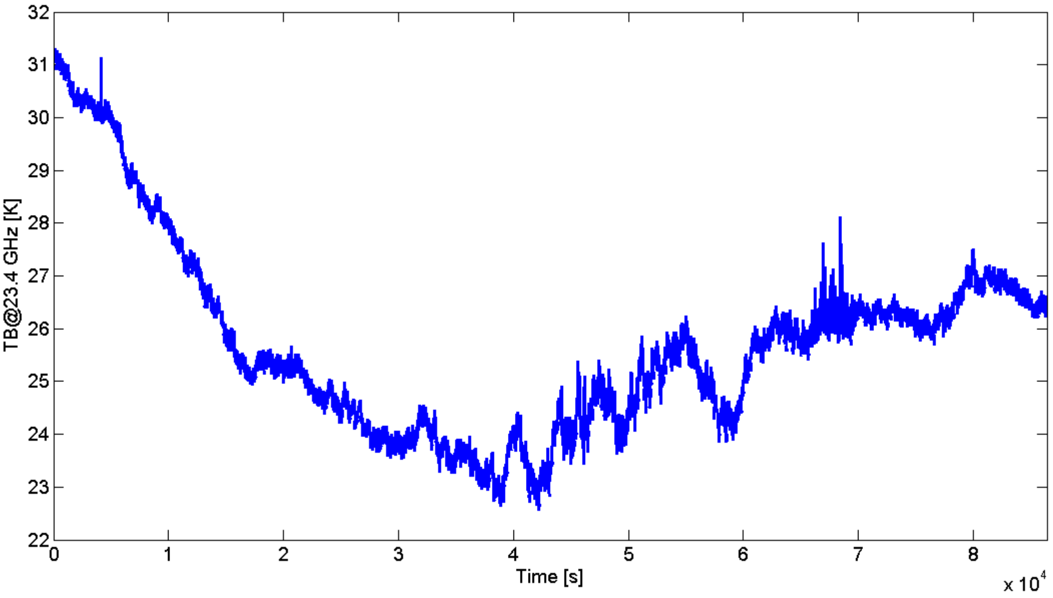

Figure 4.2: Measured brightness temperature at the 23.4 GHz channel of the ATPROP MWR

As the wet troposphere is likely not to be a major component of the ASD measured at 10 s observation time, the same quantity is comparable with the ASD measured at 100 s. Thus, a possible approach to the data analysis could consist in evaluating differences between measurements taken at defined intervals: 2, 4, 8, 16, 64 and 128 s, where the 2 s step is the instrument data output sample time.

In particular, the intrinsic noise can be assessed by computing the rms average of the differences versus the time separation, thanks to the use of the TSF. The assumption is that the instrument noise component of fluctuations is identified by the rms of the adjacent differences at 2 s. The 2 s adjacent data will be pure instrumental noise and the atmosphere effects will show up as we increase the time separation of the differencing.

Considering the ATPROP MWR data, TSF has been applied on the ATPROP data and results in terms of the ZWD and TB are reported in Figure 4.3 and Figure 4.4, respectively.

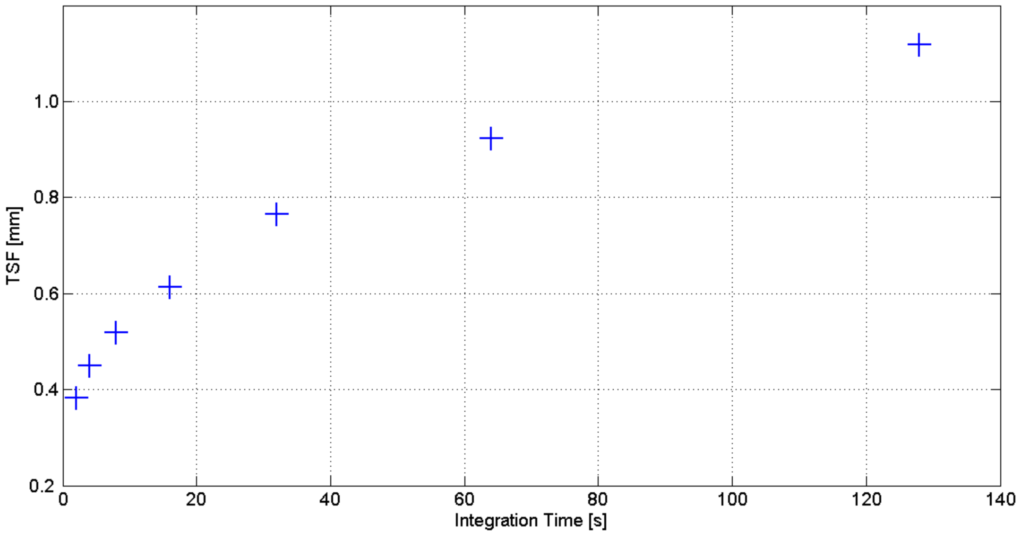

Figure 4.3: Standard deviation of the ZWD difference vs time interval for ATPROP

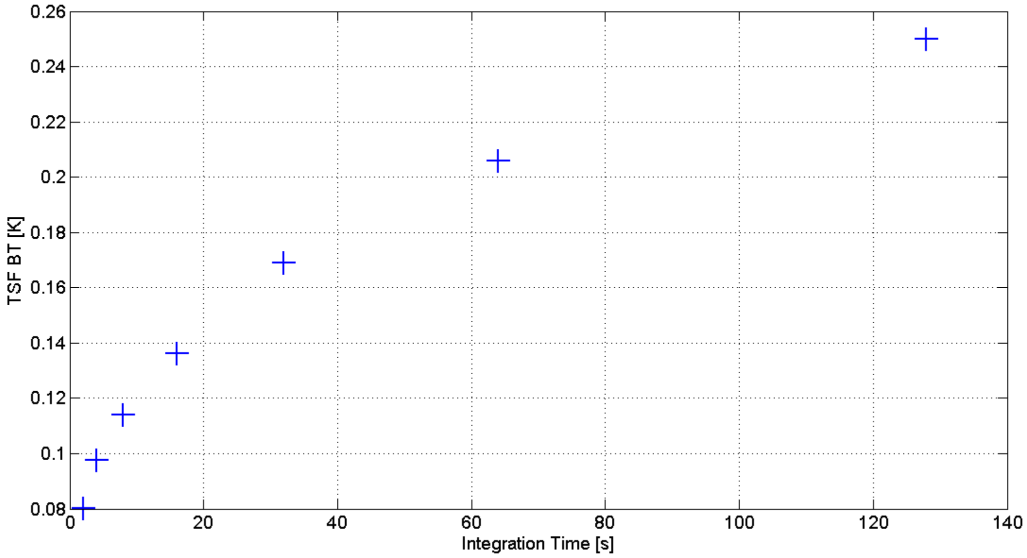

Figure 4.4: Standard deviation of the TB difference for the 23.4 GHz ATPROP channel vs time interval

The values at the 2 s interval represent the AWVR thermal noise of about 0.4 mm in Path Delay (PD) and 0.08 K in TB. These values can be interpreted as the single measurement noise values for 1 s integration time by using the TSF at an integration time of 1 s.

Results with different pointing and tracking configuration have to consider the mapping function [RD. 45] in order to scale the observation to the zenith direction.

What is also noteworthy in these plots is the rapid rise in the measured TSF beyond 2 s. In previous references [RD. 34] it was argued that the "crossing point" where the signals due to atmospheric fluctuations match the AWVR thermal noise was in the 20-30 s time interval. However, the data shown here suggests that the crossing point occurs closer to ≈8 s where the measured TSF exceeds the minimum (noise) value by $\sqrt{2}$. In assessing the crossing point where the typical atmosphere variations are equivalent to the instrument noise contribution, it is assumed that the two sources of variation (instrument noise and atmosphere) add in quadrature. Thus, an increase by a factor of $\sqrt{2}$ in the measured variability over the instrument noise contribution reflects an atmospheric contribution that matches the instrument noise. As summarized in Table 4.1 the standard deviation values of the ZWD and TB computed at 8 s are a factor of $\sqrt{2}$ of the 2 s values.

	2 s	**8 s**
ZPD [mm]	0.382	0.517
TB [K]	0.080	0.114

Table 4.1: Standard deviation values of the ZWD and TB at 2 s and 8 s

The standard deviation of the ZWD obtained with the TSF at 2 s has been used to estimate the ASD of the data. In particular the value has been used as input for the Simplified Allan Standard Deviation (SASD) [AD. 7].

Figure 4.5 shows the results of the two ASD formulation. Blue curve represents the standard ASD while the green curve is the SASD considering the ZWD TSF value at 2 s as input. As detailed in [AD. 7], the SASD can be used for observation time up to 1000 s, for this reason the two curves have different length.

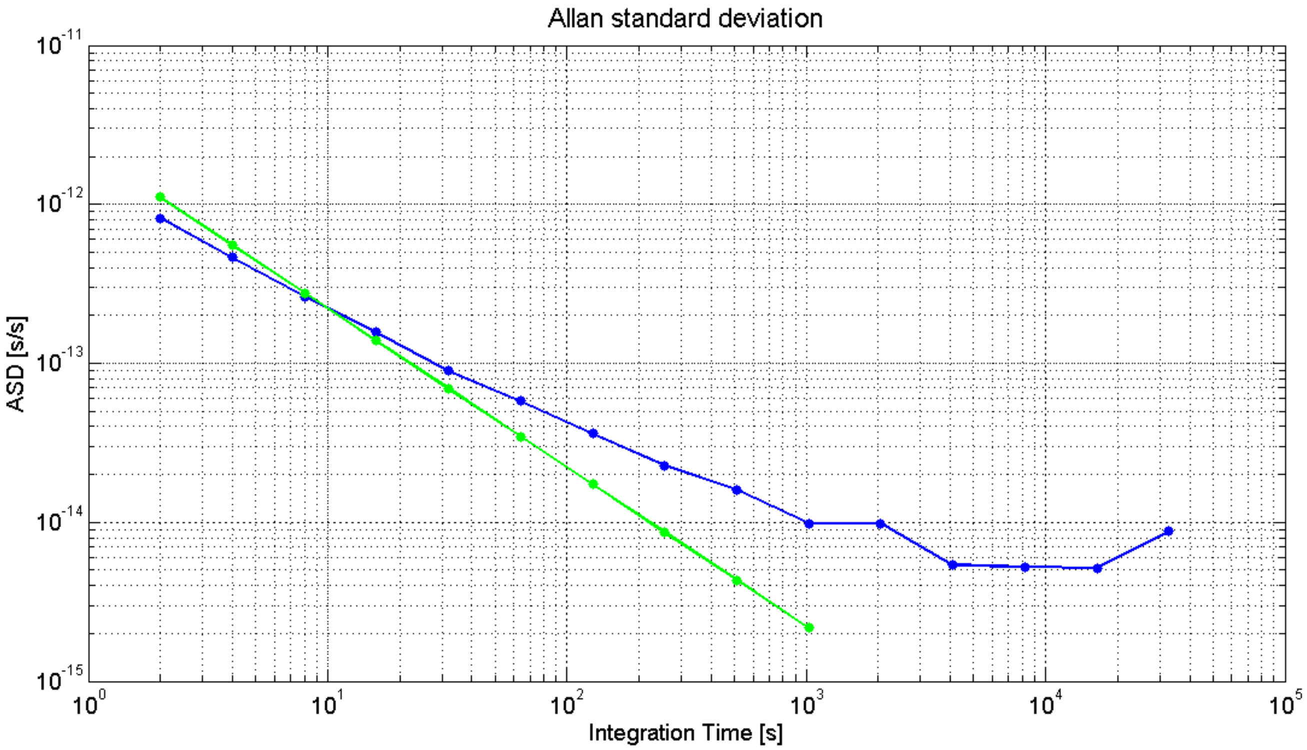

Figure 4.5: Comparison of the ASD for the selected data set. Blue curve has been obtained with the standard ASD formulation, green curve has been obtained with the SASD formulation considering the TSF of the standard deviation of the ZWD computed at 2 s as input value

It results that for short observation time the noise level computed with the SASD is greater than the standard ASD. The inversion trend occurs at 10 s observation time, where the SASD estimates lower noise level.

In order to evaluate the goodness of the analysed data, Figure 4.6 shows the comparison of the TSF results (blue stars) and the Treuhaft – Lanyi (TL) model [RD. 74] (red line).

The TSF produces too large values for the wet delay variation of data set at 128 s. If a large enough data set has been used (~days) it is reasonable to expect that the atmospheric variability on all time scales (1 -100s) are deviating from the TSF model in a similar way. The TL model can be scaled to fit the data at greater time scales. In Figure 4.6 a down-scaling of the TL-model by a factor of about 1.8, would make the red and blue curves meet at 128 seconds. At the same time the scaled TL-model predicts a 1.8 times smaller value also for 2 s. At 2 s the instrumental noise can be obtained by subtracting the expected variance (scaled TL-model) from the measured variance, and divide by 2, since a value of 2*(noise variance) in the difference data is obtained. The scaling of the rms TL model curve corresponds to a down-scaling of the C_{n^2} parameter by 1.8^2.

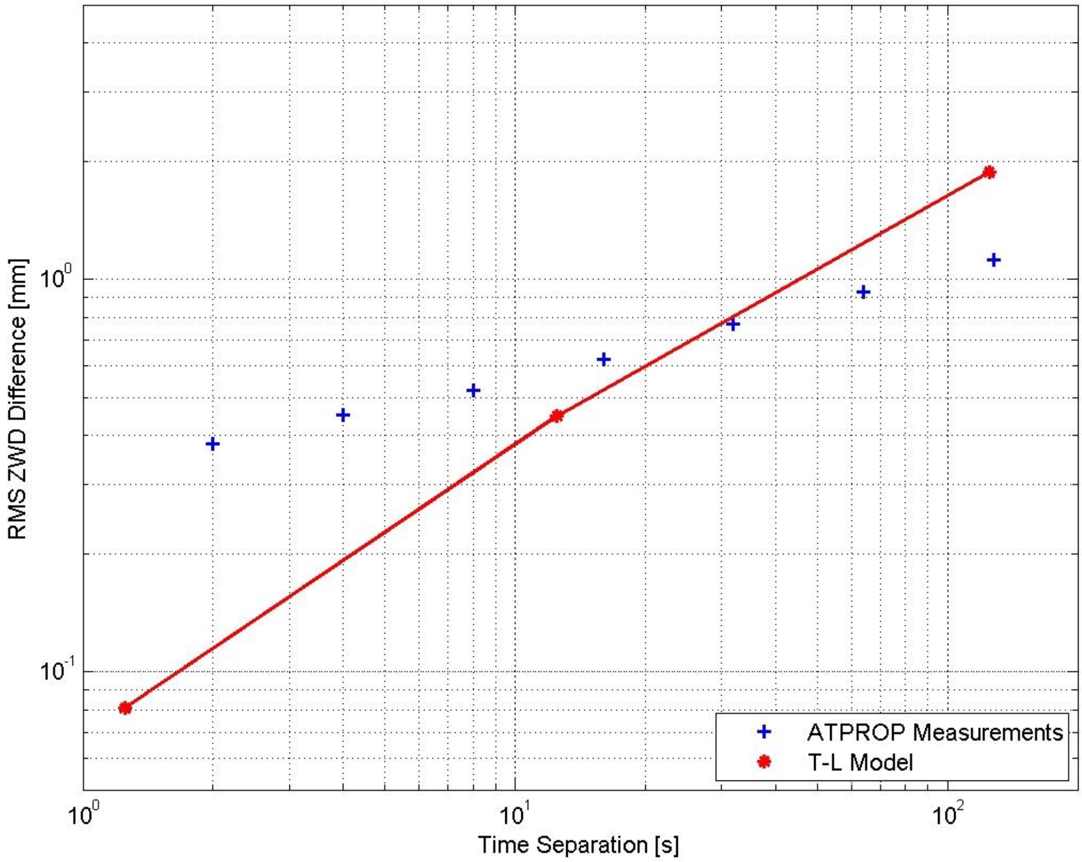

Figure 4.6: Comparison between the TSF and the Treuhaft – Lanyi model of the differenced ZWD

4.2 Difference Procedure

This technique is based on the use of two different MWR installed in the same area (close to each other) and pointing in the same direction. This method has been named “Difference Procedure” because it has been based on the difference between the measurements of the two instruments. The main hypothesis of this procedure is that apart from all possible instrumental differences, the two instruments are observing the same atmosphere.

For each instrument, the estimated PD is the sum of two contribution: the PD due to the atmosphere, PD_{atm}, and a contribution due to the instrumental internal noise, PD^I. In general the two instruments have been defined A and B, where A is the instrument to be characterized.

$$\left.\begin{aligned} PD_A &= PD_{atm} + PD_A^I \\ PD_B &= PD_{atm} + PD_B^I \end{aligned}\right\} \tag{4-1}$$

The procedure is based on the use of the ASD of the difference of the two instruments PD. This means that, according to the previous hypothesis, the tropospheric contribution cancels out while we remain only with the sum (in a quadratic sense) of the instrumental internal noise.

$$\Delta ASD_{AB}(\tau) = ASD(PD_B(t) - PD_A(t)) \tag{4-2}$$

The ASD of the difference of the two signals is defined as:

$$\Delta ASD_{AB}(\tau) = \sqrt{ASD_B^I(\tau)^2 + ASD_A^I(\tau)^2} = ASD_A^I(\tau)^2 \cdot \sqrt{N^2+1} \qquad (4\text{-}3)$$

Where ASD_A^I and ASD_B^I are the ASD due to internal noise of instrument A and B respectively and N is the ratio of the ASD's of the internal noise of both instruments, defined as: $N = ASD_B^I / ASD_A^I$.

It has been assumed that the ratio N is independent of time lag τ . This is verified if internal noise is white noise and its ASD follows a τ^{-1} power law. Our investigation showed that ΔASD follows a τ^{-1} power law indicating that both ASD_A and ASD_B are following a τ^{-1} power law. For this reason the assumption of N being constant is reasonable.

It is further assumed that the total ASD derived from the signal measured by the instrument is dominated by the instrumental internal noise for small observation time:

$$ASD(\tau_0) \cong ASD^I(\tau_0) \qquad (4\text{-}4)$$

Thus the ratio N can be derived from the ASD at the smallest available observation time τ_0 which coincide with the time series time step.

Computing the ASD of the signal measured by the two instruments at the same (short) integration time τ_0 , the ratio N can be computed as:

$$N = N_0 = {ASD_B(\tau_0)} \Big/ {ASD_A(\tau_0)} \qquad (4\text{-}5)$$

To summarize, this method is based on three assumptions:

a. In the ASD of the difference of both instruments atmospheric fluctuations cancel out. If instruments are close to each other and the distance relative to the volume they sample the atmospheric signal is small the atmospheric signal should be the same and cancel. As the ASD of the difference signal follows a τ^{-1} power law the difference signal is white noise: probably the sum of the internal noise of both instruments.

b. N is a constant because ΔASD follows a τ^{-1} power law, which means that ASD_A^I and ASD_B^I follows a τ^{-1} power law

c. $ASD(\tau_0) \cong ASD^I(\tau_0)$: the ASD of the dataseries at the smallest time step is dominated by ASD of the instrumental noise.

4.3 White Noise Procedure

This procedure is based on the use data of a single instrument and the assumption that the internal noise is a pure White Gaussian Noise (WGN). For this reason this procedure has been named “White Noise Procedure” (WNP).

For this procedure two assumptions have been considered:

a. Instrumental noise is WGN and thus follows a τ^{-1} power law.

b. $ASD(\tau_0) \cong ASD^I(\tau_0)$ which means that the ASD of the dataseries at the smallest time step is dominated by ASD of the instrumental noise, where $\tau_0 = 1s$ (the smallest data series time step).

Putting these two assumptions together, the ASD of the instrumental noise at any time step is:

$$ASD(\tau) = ASD(\tau_0) \cdot \left(\frac{\tau}{\tau_0} \right)^{-1} \tag{4-6}$$

It should be noted that the crucial aspect of this method is that the time series should be acquired in clear sky conditions where at short integration time ASD is dominated by the instrumental noise fluctuations.

In practice, defining $\tau_0 = 1s$ and $\tau^* = 4s$ or $20s$, the following procedure has been implemented:

a. Compute the ASD of the MWR time series at 1s integration time.

b. Use the $ASD(\tau_0)$ as the standard deviation of a WGN.

c. Use the value of the $ASD(\tau_0)$ as input for the WNP, Equation (4-6).

d. Compute the standard deviation at different integration time: $\sigma(\tau^*) = \sigma(\tau_0 = 1s) / \sqrt{\tau^*}$

e. Use the $\sigma(\tau^*)$ in the SASD formulation to compute the $ASD(\tau^*)$

f. Use the values of the $ASD(\tau^*)$ as input for the WNP, Equation (4-6).

It should be noted that once the procedure has been tested and validated only the integration at 20s will be considered.

5 REVIEW OF MODELING AND REMOTE SENSING TECHNIQUES FOR THE EFFECT OF ATMOSPHERIC TURBULENCE

Turbulence is an important effect for many different applications including different aspects of electromagnetic propagation in the atmosphere. In our application we are interested in the effect for frequencies in the microwave part of the spectrum. The parameter of interest is an integrated effect, namely the propagation delay of a signal propagating through the Earth's atmosphere to a receiver on the ground. As described in the statement of work (SOW) [AD. 1] and in [RD. 40] the variations in the propagation delay in the microwave region is dominated by water vapour. Therefore, in this chapter the focus will be on the wet refractivity and the wet delay. However, given that the requirement is to correct at least for 90% of this wet delay, the residual part is approaching the level where the variations in the dry refractivity (mainly temperature variations) may start to become important. Therefore, we will also try to mention all available techniques in our review of remote sensing instruments that can be used to detect and monitor atmospheric turbulence.

For systems where calibration for the wet delay is done by means of radiometric measurements there is usually an uncalibrated remainder of the variability due to imperfections in the method. The radiometer location, the pointing on the sky and an extended beam width can deviate from the desired. There could also be residuals due to assumptions about the atmospheric variability when the instrument is calibrated. In this chapter we present statistical models for the wet delay variability, give examples of error calculations based on the models, and review means of deriving model parameters from remote sensing techniques.

5.1 Statistical Measures of Atmospheric Delay Variations

We start by presenting some statistical measures that will be used in the following.

5.1.1 Spatial Variations Measures

Often in the modelling the atmosphere is assumed to be homogeneous, *i.e.*, the structure function is independent of the starting point $\vec{r}$. If, furthermore, the variations are statistically independent of the direction of the separation R, the atmospheric medium is said to be isotropic. This is often the case for small separations. We can then write the structure function, Equation, as dependent on one variable $R = |\vec{R}|$ only:

$$D_{n(R)}(\vec{R},\vec{r}) = D_{n(R)}(R) \tag{5-1}$$

A slant atmospheric delay structure function can be defined similarly. For a site at $\vec{s}$ observing along a path with elevation and azimuth angles θ, φ we define the structure function for a horizontal separation $\vec{R}$ as

$$D_{l(R)}(\vec{R},\vec{s};\theta,\varphi) = [def] = E\{(l_{\theta,\varphi}(\vec{s}+\vec{R}) - l_{\theta,\varphi}(\vec{s}))^2\} \tag{5-2}$$

For a homogeneous isotropic medium an expression based on the refractivity structure function can be derived from vertical integration:

$$D_{l(R)}(\vec{R};\theta,\varphi)=\frac{1}{\sin^{2}\theta}\cdot\iint[D_{n(R)}(|(\vec{r}(v)+\vec{R})-\vec{r}(v')|)-D_{n(R)}(|(\vec{r}(v)-\vec{r}(v')|)]dvdv' \qquad (5\text{-}3)$$

Where $\vec{r}(v)$ are positions along the line of sight (see [RD. 74] is where it is applied in order to derive the wet delay structure function). In order for the integration to converge an upper limit for the vertical coordinate is often introduced (Treuhaft and Lanyi integrated up to 1000 m). An alternative approach could be to make $D_{n(R)}$ a function of the height [RD. 22].

We will also use the variance of the difference, $E\{(l_A-l_B)^2\}$, to compare two slant wet delays when the paths A and B are in different directions, as well as possibly starting in different points as the ground. In this case we cannot describe the path difference by a single displacement vector. To make their mean values equal we scale the original slant delays, $l_{A,0}$ and $l_{B,0}$, to their equivalent value at a desired elevation angle θ_{ref} and get, $l_A=\frac{\sin\theta_A}{\sin\theta_{ref}}\cdot l_{A,0}$.

The variance of the difference can now be calculated using integration of the refractivity structure function (assuming a homogeneous isotropic medium):

$$\begin{gathered}E\{(l_A-l_B)^2\}=\\ \frac{1}{2\sin^{2}\theta_{ref}}\cdot\iint[2D_{n(R)}(|\vec{r}_A(v)-\vec{r}_B(v')|)-D_{n(R)}(|(\vec{r}_A(v)-\vec{r}_A(v')|)-D_{n(R)}(|(\vec{r}_B(v)-\vec{r}_B(v')|)]dvdv'\end{gathered} \qquad (5\text{-}4)$$

where $\vec{r}_A(v)$ and $\vec{r}_B(v)$ are positions along the paths A and B respectively.

The derivation of the structure function is reported in Annex A.1.

5.1.2 Temporal Variation Measures

To study delay rate variations we can use the dimensionless Allan Variance (AV) of the frequency [RD. 3]. In this case the delay is expressed in units of time: $[l(t+\tau)-l(t)]/c$, where c is the speed of light:

$$A_f^2(\tau)=E\left\{\frac{[[l(t+\tau)-l(t)]/c-[l(t)-l(t-\tau)]/c]^2}{2\tau^2}\right\} \qquad (5\text{-}5)$$

The results can also be presented as ASD as $A_f(\tau)=\sqrt{A_f^2(\tau)}$. It should be noted that there are a couple of alternative formulations of the AV with different statistical properties [RD. 13]. The definition presented in Equation (5-5) is often referred to as AV, and the accompanying ASD. By using:

$$\begin{gathered}[[l(t+\tau)-l(t)]-[l(t)-l(t-\tau)]]^2=\\ 2\cdot[l(t+\tau)-l(t)]^2+2\cdot[l(t)-l(t-\tau)]^2-[l(t+\tau)-l(t-\tau)]^2\end{gathered} \qquad (5\text{-}6)$$

we can rewrite the Allan Variance using the delay structure functions as:

$$A_f^2(\tau) = \frac{1}{2c^2\tau^2}\cdot E\left\{4\cdot\left[l(t+\tau)-l(t)\right]^2-\left[l(t+\tau)-l(t-\tau)\right]^2\right\} = \frac{1}{2c^2\tau^2}\cdot\left[4\,D_{l(\tau)}(\tau)-D_{l(\tau)}(2\tau)\right] \tag{5-7}$$

5.2 Atmospheric Variation Models

5.2.1 Spatial Variability Models

A starting point for a derivation of the statistical variations of the atmospheric delay is Kolmogorov's work on the kinetic energy in the atmospheric wind field [RD. 71] [RD. 80]. By assuming that kinetic energy is fed into the circulation at relatively large spatial scales, and then the energy in the larger eddies is transferred to smaller and smaller eddies without energy loss until, finally, the energy is dissipated as heat due to the viscosity. If it can be assumed that the energy transfer to smaller spatial scales lasts for several orders of magnitude in an isotropic medium possible structure functions can be identified through a dimensional analysis [RD. 71]. The resulting wind velocity structure function for an inertial range is:

$$D_v(R) = C_v^2 \cdot R^{2/3} \qquad R_i < R < R_o \tag{5-8}$$

where C_v^2 is a constant. The inner limit R_i is on a scale from mm to cm. Structure functions with a power law index of approximately 2/3 have been confirmed in a wide range of experiments [RD. 80]. Small modifications of the power law index has, however, been discussed, e.g. due to the fact that the energy dissipation is intermittent [RD. 4]. For larger spatial scales beyond R_o, say larger than 1 km, the wind field tends to be two-dimensional and we reach scales where energy can be expected to be injected. On these scales there are several possible assumptions for modelling the flow. Different models have been investigated using simulations, [RD. 12], [RD. 68].

Structure functions of other atmospheric quantities can be derived from models of the wind dynamics. The humidity as well as the temperature follows the flow [RD. 71], [RD. 37]. Temperature fluctuations are the dominant cause of hydrostatic refractivity fluctuations [RD. 80]. This means that for both the wet refractivity and the hydrostatic (dry) refractivity components a number of structure functions similar to Equation (5-8), with power law indices of 2/3, can be found. Treuhaft and Lanyi suggest the following wet refractivity structure function [RD. 74]:

$$D_{n(R)}(R) = C_n^2 \cdot R^{2/3} \cdot [1+(R/R_s)^{2/3}]^{-1} \tag{5-9}$$

where C_n^2 is a constant describing the strength of the variability in the wet refractivity. A value $C_n^2 = 5.76\times10^{-14}\ \mathrm{m}^{-2/3}$ is suggested for an average variability [RD. 74]. The factor in the square brackets ensures that the structure function at large enough separations reach a saturation value. By integrating this equation using Equation (5-3) we get the corresponding wet delay structure function. An example of this is shown in Figure 5.1. The shape of the function can be described as:

$$D_{l(R)}(R) \propto R^{\alpha} \tag{5-10}$$

where the power-law index α change with R, and has the following asymptotes:

$$\alpha = \begin{cases} 5/3 & R \ll H \\ 2/3 & H \ll R \ll R_s \\ 0 & R \gg R_s \end{cases} \tag{5-11}$$

with smooth transitions between these intervals. In [RD. 74] the upper limit for the vertical integration, H, is set to 1000 m, and R_s, the saturation distance, is set to 3000 km in order to fit observational data. See next section for a comment on the latter choice.

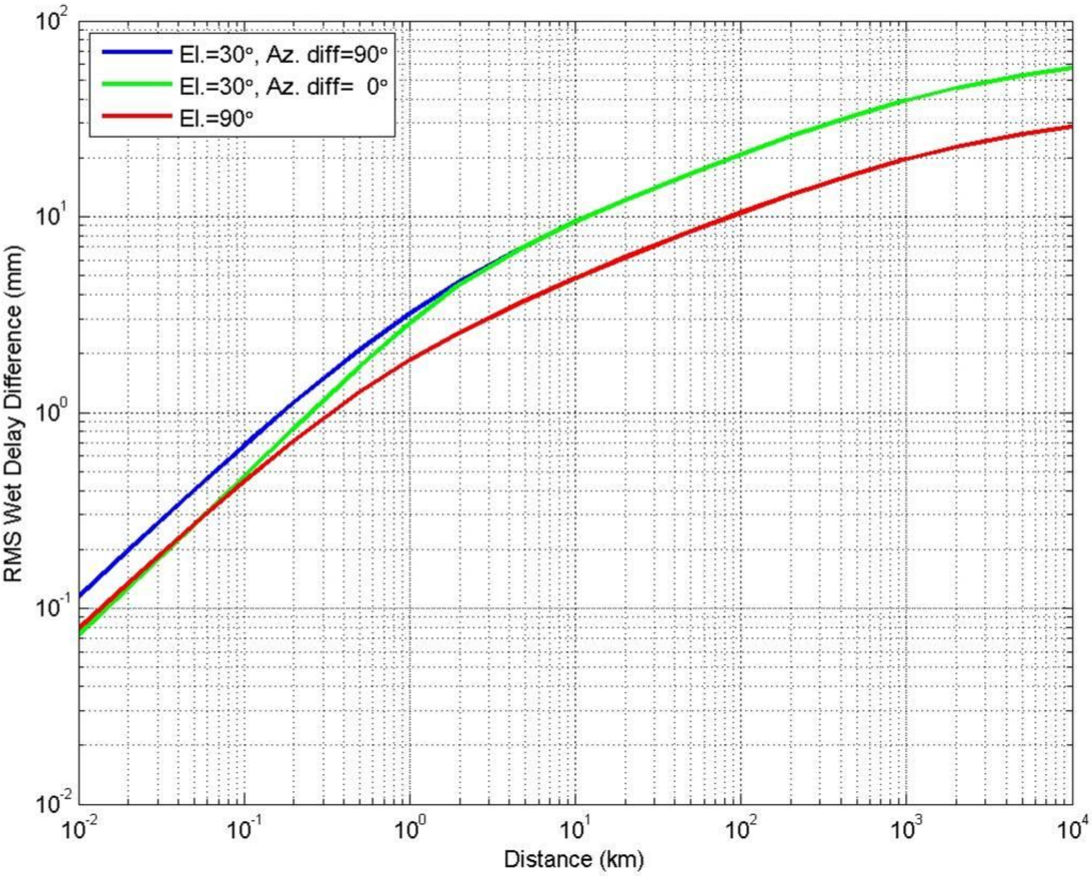

Figure 5.1: The RMS wet delay differences, the square roots of the spatial wet delay structure functions, for a couple of observation directions relative to the separating baseline. The model by Treuhaft and Lanyi has been used in the calculations

5.2.2 Temporal Variability Models

A way to introduce a temporal model for the atmospheric variability is to assume that a spatial structure is flowing over a site with a wind velocity without changing its structure. This "frozen flow hypothesis" is described in [RD. 80]. We can thus reuse the spatial models for time separations and get the models of the refractivity structure function as

$$D_{n(\tau)}(\tau) = D_{n(R)}(v \cdot \tau) \tag{5-12}$$

and equivalently, obtain the delay structure function model of the delay from

$$D_{l(\tau)}(\tau;\theta,\varphi) = D_{l(R)}(v\cdot\tau;\theta,\varphi) \tag{5-13}$$

for a wind velocity v. A combination of spatial and temporal separations $\vec{\rho} = \vec{R} - \vec{v}\cdot\tau$ can also be used. The frozen flow hypothesis should be used with some caution for longer time lags. In general we can expect that if we follow the wet delay using an average wind vector $\vec{v}$ for a long stretch with $\vec{R} = \vec{v}\cdot\tau$ it will change significantly, *i.e.*

$$l_{\theta,\varphi}(\vec{r}+\vec{R},T=t+\tau) \neq l_{\theta,\varphi}(\vec{r},T=t) \tag{5-14}$$

This is due to ongoing evaporation and condensation, as well as local variations in the wind field. The wind vector typically changes both its direction and size with height in the lower atmosphere [RD. 25]. On shorter time scales the hypothesis can in general describe the temporal variability well, see [RD. 36] for a discussion.

Treuhaft and Lanyi [RD. 74] have suggested a wind velocity of 8 m/s for a model of the average temporal variability using the frozen flow hypothesis. The spatial wet delay structure functions in Figure 5.1 can also be seen as a temporal one after reinterpreting the x-axis as a time axis. After “infinite time” the wet delay should be uncorrelated, thus a structure function $D_{l(\tau)}(\infty) = 2\sigma_l^{\ 2}$ where $\sigma_l^{\ 2}$ is the wet delay variance. The value 3000 km for R_s in Equation (5-9) is chosen so that $D_{l(\tau)}(\infty) = 1.2\cdot 10^{-3}$ m^2 which gives σ_l =24 mm, corresponding to the annual wet delay fluctuations at mid-latitudes [RD. 74].

The ASD for the wet delay variations of the Treuhaft and Lanyi model is presented in Figure 5.2 for some directions of observation. Note the significant difference between the results when observing along and perpendicular to the wind direction. It also shows that without external corrections the atmospheric variability is expected to be too large for the design criteria to be met.

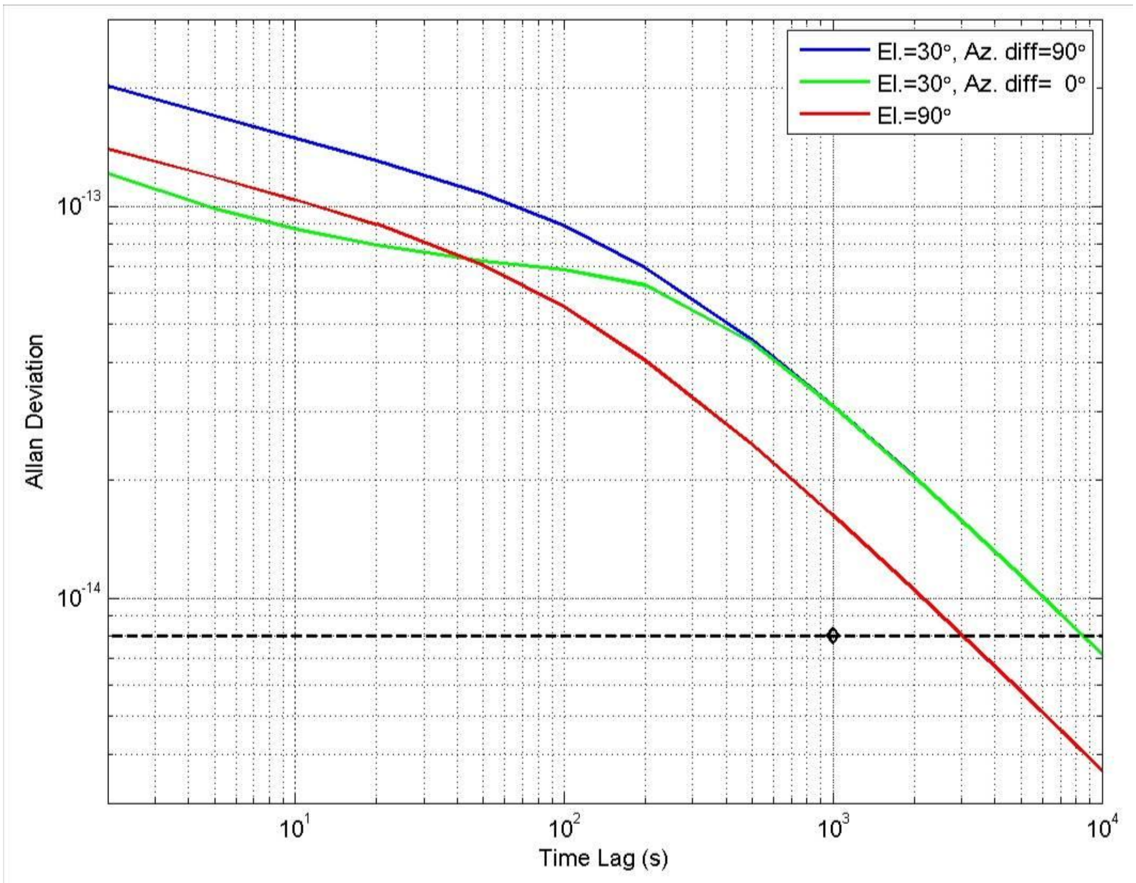

Figure 5.2: Allan deviation due to wet delay variation for a couple of observation directions relative to the wind direction. The model by Treuhaft and Lanyi has been used in the calculations. The study's design criteria, an Allan deviation of $8 \cdot 10^{-15}$ at 1000 s, is denoted by a diamond.

5.2.3 Variations in the Statistical Parameters

The models for refractivity and delay variations that originate from theoretical work or simulations often lack information on the absolute sizes of the effects. They merely present possible shapes of the functions, *e.g.*, of the structure functions. Parameters need to be derived from measurements, as described below. They vary significantly with time, since the general atmospheric conditions change. [RD. 47] presents spatial wet delay structure function results from a GPS network in Nevada, USA. The derived strength parameter has a strong seasonal dependence; summer and winter values differ by up to a factor 10. Similar variations in the strength parameter are also seen for Scandinavian data [RD. 30]. Large variations in strength parameters are also presented in several of the articles reviewed in the section on Remote Sensing Techniques below. This calls for regular monitoring of the parameters in order to apply the models with some precision, e.g., in the delay error budget calculations.

5.3 Application of Turbulence Models in Radiometric Data Analysis

When calibrating a desired slant atmospheric delay using measurement data the error may not only be due to the instrument; a remnant due to the atmospheric variability could also be present. Two main reasons for this effect are:

- data are not acquired in the desired line of sight, or at the correct time
- instrumental calibration (*e.g*. radiometer tip-curve analysis) can be affected by atmospheric variations

The deviation from the desired line of sight for radiometer data acquisition is due to one or several of the following reasons:

- the antenna beam is too wide
- offset site position of the radiometer with respect to the observations that are to be calibrated
- offset pointing of the radiometer on the sky, *e.g.*, in order to avoid radiation from the sun or the ground

Below we present example calculations of these three effects. The examples can be regarded as illustrations of possible investigations when a refractivity model with appropriate parameter values is at hand. We have used the Treuhaft and Lanyi model with standard parameter values. In graphs where we present RMS errors we mean $\sqrt{E\{(l_A - l_D)^2\}}$.

In some applications we may consider a desired wet delay, l_D , which is approximated by an alternative, l_A , which is a sum of delays

$$l_A = \sum w_p \cdot l_p \tag{5-15}$$

where $\sum w_p = 1$ (we assume that the delay already has been scaled to the desired elevation angle). In such cases the variance of the wet delay difference can be calculated using

$$\begin{aligned} &E\{(l_A - l_D)^2\} = \\ &\sum_p w_p \cdot E\{(l_p - l_D)^2\} - ½ \cdot \sum_p \sum_q w_p w_q \cdot E\{(l_p - l_q)^2\} \end{aligned} \tag{5-16}$$

The derivation of this equation is reported in Annex A.2.

We can also examine the AV of the residual delay $\Delta l = l_A - l_D$ where l_D . Following Equation (5-7) we get:

$$\begin{aligned} &A_f^2(\tau) = \frac{1}{2c^2\tau^2} \cdot E\left\{4 \cdot [\Delta l(t+\tau) - \Delta l(t)]^2 - [\Delta l(t+\tau) - \Delta l(t-\tau)]^2\right\} = \\ &\frac{1}{2c^2\tau^2} \cdot E\left\{4 \cdot [\Delta l(t+\tau) - \Delta l(t)]^2 - [\Delta l(t+2\tau) - \Delta l(t)]^2\right\} \end{aligned} \tag{5-17}$$

The terms, with the common form $E\left\{[\Delta l(t+n\tau) - \Delta l(t)]^2\right\}$, can be calculated using expansions of Δl into squared components of l_A and l_D :

$$\begin{aligned}
&[\Delta l(t+n\tau)-\Delta l(t)]^2 = [[l_A(t+n\tau)-l_D(t+n\tau)]-[l_A(t)-l_D(t)]]^2 = \\
&[l_A(t+n\tau)-l_D(t+n\tau)]^2 + [l_A(t)-l_D(t)]^2 + \\
&[l_A(t+n\tau)-l_A(t)]^2 - [l_A(t+n\tau)-l_D(t)]^2 - [l_D(t+n\tau)-l_A(t)]^2 + [l_D(t+n\tau)-l_D(t)]^2
\end{aligned} \qquad (5\text{-}18)$$

The AV is then calculated from the expectation values of the terms in Equation (5-18) entered into Equation (5-17).

5.3.1 Beam Width Influence

We simulated a beam by a set of paths evenly spread around the desired pointing. We used 7 concentric circles and 8 line-of-sight directions evenly spread on each circle. We regarded the wet delay measured by the antenna as a weighted sum of these 56 observations, $l_A = \sum w_p \cdot l_p$. The weights were derived using an assumed Gaussian beam shape. We then used Equation (5-16) to calculate an RMS error. We repeated the calculations for a set of different beam widths. The results are shown in Figure 5.3.

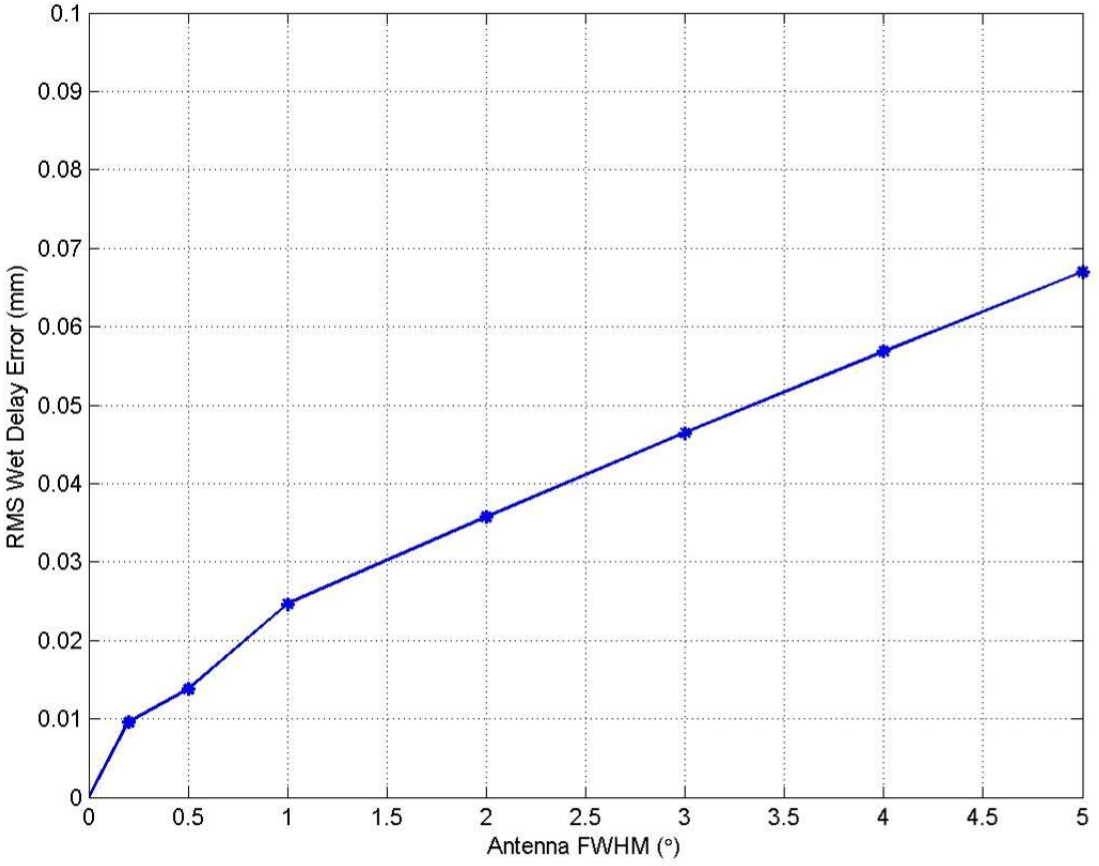

Figure 5.3: The expected deviation of the wet delay seen in a wide beam from the wet delay along a straight line in the beam center. The pointing is in the zenith direction. The RMS deviation is presented as a function of the full-width-half-maximum antenna beam width for a Gaussian beam

One problem with this calculation is that the different lines will have different elevation angles and therefore should have different mean values (Equation (5-16) assumes that all delays have identical mean values). We choose the zenith direction as the desired pointing in order to use the equation without making a too large error. There is a systematic effect of broader beams observing greater expected mean delay in the beam than a narrower beam. This is a consequence of the asymmetry in path delay as a function of elevation. We illustrate this effect in Figure 5.4.

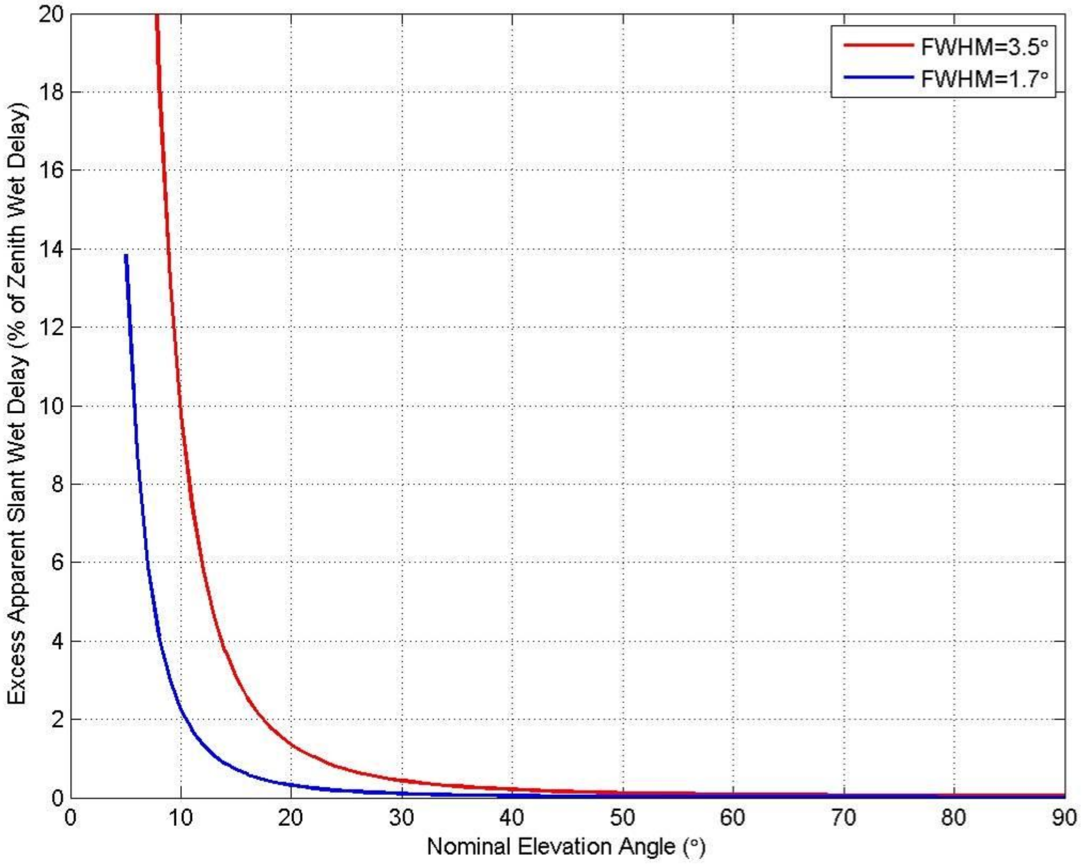

Figure 5.4: Expected excess mean value of the wet delay in a Gaussian beam, when compared to an ideal beam with zero width. Mean delay grows rapidly towards lower elevations. A consequence is that the delay deviation from the lower parts of a broad beam exceeds the deviation in the upper part of the beam

5.3.2 Site Position Offset Influence

A radiometer at a slightly offset position (from the desired site to be calibrated) that observe in the desired direction creates data with errors described by the structure function in Equation (5-2). Figure 5.5 presents the error introduced for 0-300 m separation.

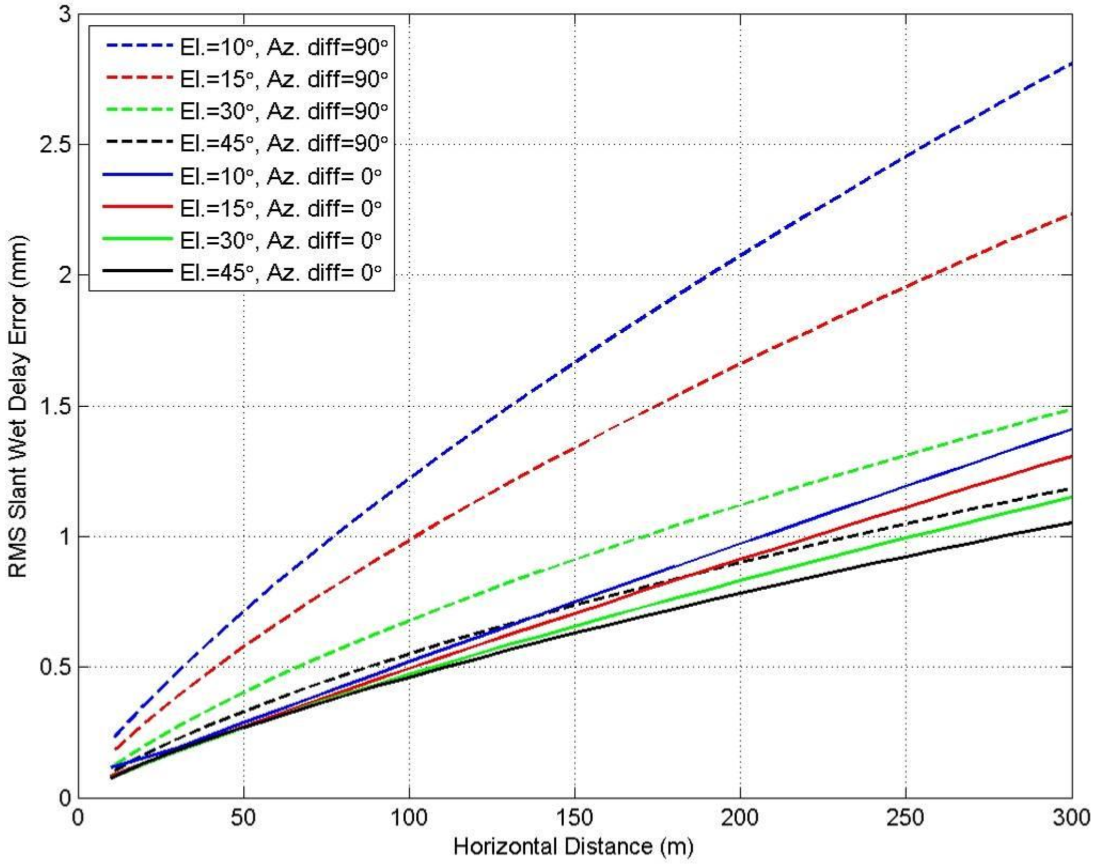

Figure 5.5: The spatial wet delay structure function for a set of observation directions. The model by Treuhaft and Lanyi has been used in the calculations. The azimuth difference angle of 90º denotes observations perpendicular to the vector of the horizontal separation, and 0º along the separation vector.

It is interesting to note that for observations acquired “along the separation vector” the error is relatively insensitive to the elevation angle. This is a consequence of two effects: at low elevations the path is longer and the slant delay variations larger, but the two separated lines are actually approaching each other at lower elevation angles for observations along the separation vector.

The distance between the radiometer and the DSA is suggested to be about 25 m (with a minimum value of 20 m, and a maximum value of 60 m) [AD. 8]. The resulting expected Allan deviations is presented in Figure 5.6. The calculations are made assuming that the radiometer is to the south of the DSA, the direction of observations is to the east, and the wind direction is to the north, a combination of directions that give large Allan deviations.

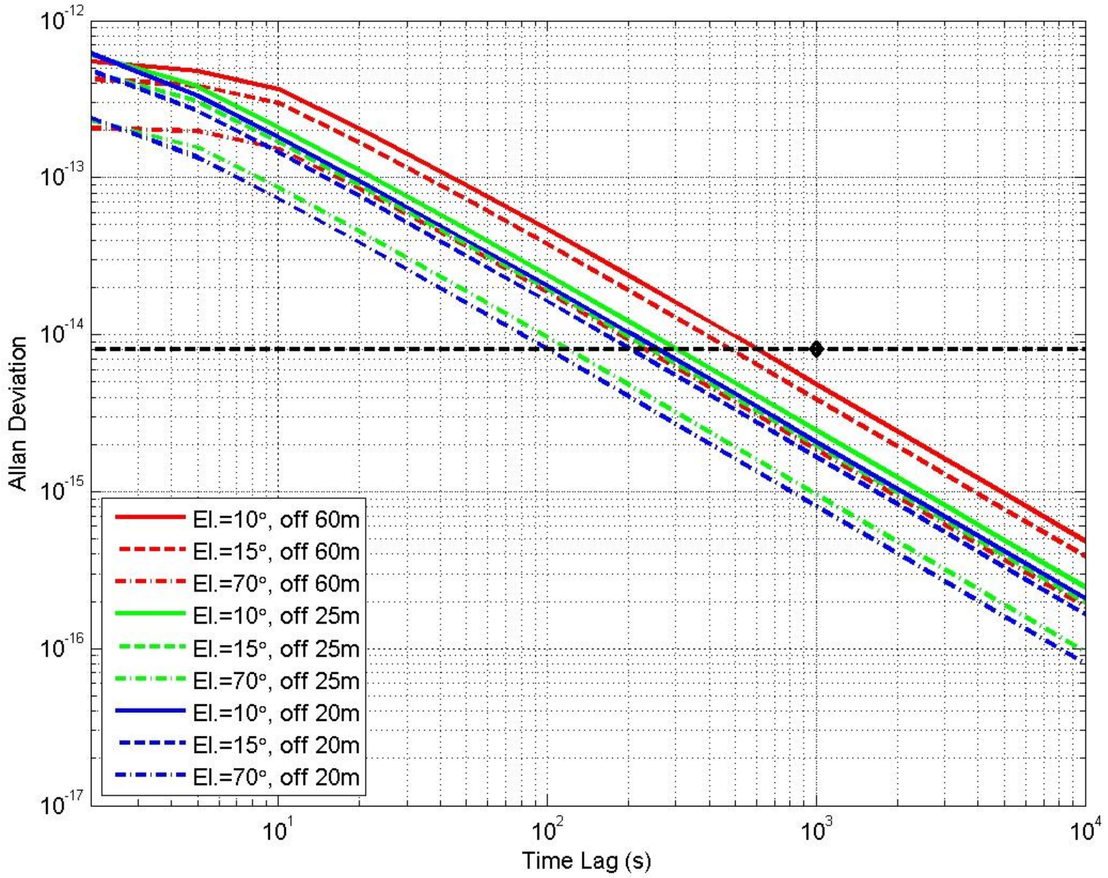

Figure 5.6: The Allan deviations due to the wet delay difference between a desired site and one located 20, 25 and 60 m to the south for observations with elevation angles 10º, 15º and 70º and azimuth angle 90º. The assumed wind direction is to the north. The study's design criteria, an Allan deviation of 8•10-15 at 1000 s, is denoted by a diamond.

5.3.3 Pointing Offset Influence

The orbit of Mercury is such that it is observed in the vicinity of the sun relatively often; the maximum angular separation is approximately 20°. For a radiometer with a significant beam width this poses problems for direct observations of the path towards the Mercury probe. In order to avoid radiation from the sun entering the radiometer beam a deliberate pointing off the direction to the S/C could be preferable. This gives, however, rise to an error in the wet delay data intended for calibrating the path towards the Mercury probe. The expected deviation from a desired delay can be calculated from a wet refractivity model. We used the model defined by Treuhaft and Lanyi to quantify the effect for a couple of pointing offsets, see Figure 5.7.

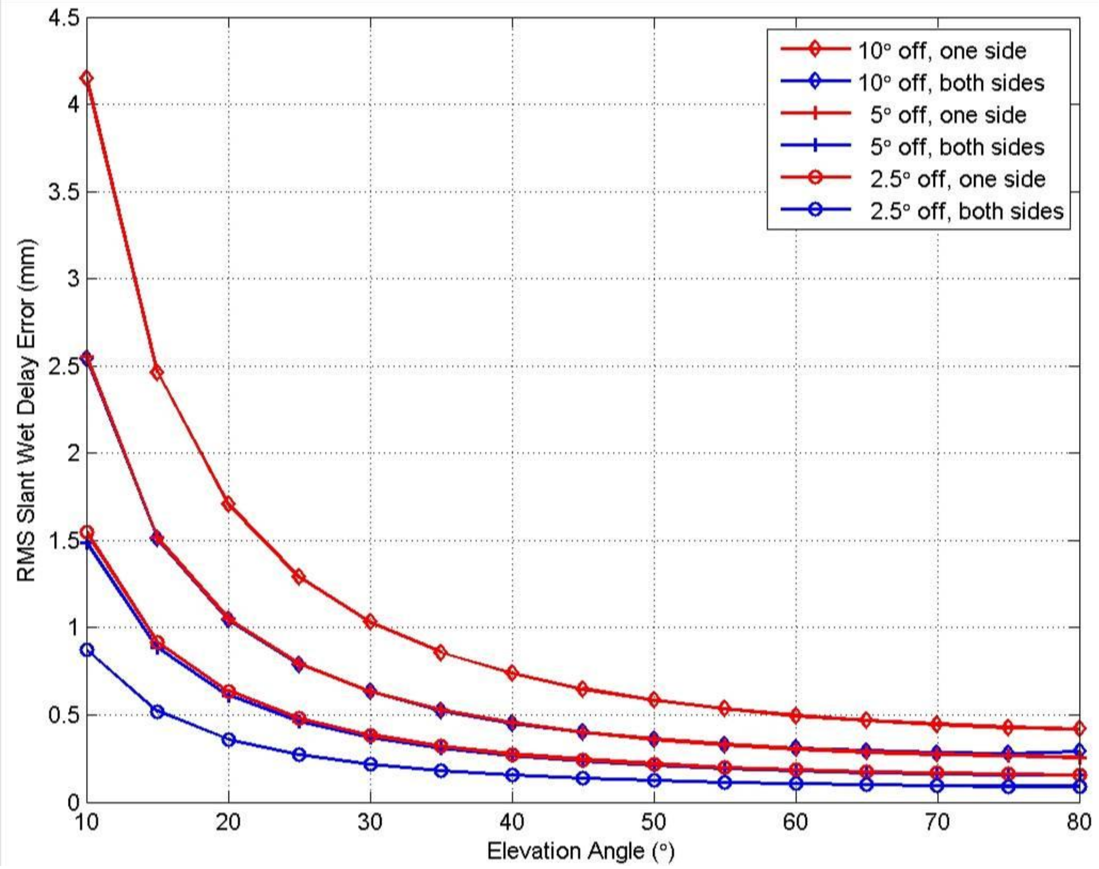

Figure 5.7: The expected deviation of a slant wet delay observed in a direction slightly different from the desired one. The effect was tested for pointing offsets with angle differences of 2.5º, 5º, and 10º, but identical elevation angle for the measured and the desired pointing. The model by Treuhaft and Lanyi and an assumed wind direction perpendicular to the observational directions has been used in the calculations. We have also calculated the deviation when the mean of two measurements on each side of the desired pointing is used (marked as "both sides).

Comparisons can be made between the Allan deviations for the wet delay itself and for the wet delay residuals when calibrating the delay with data acquired with a pointing offset. Figure 5.8 shows an example for relatively low elevation observations.

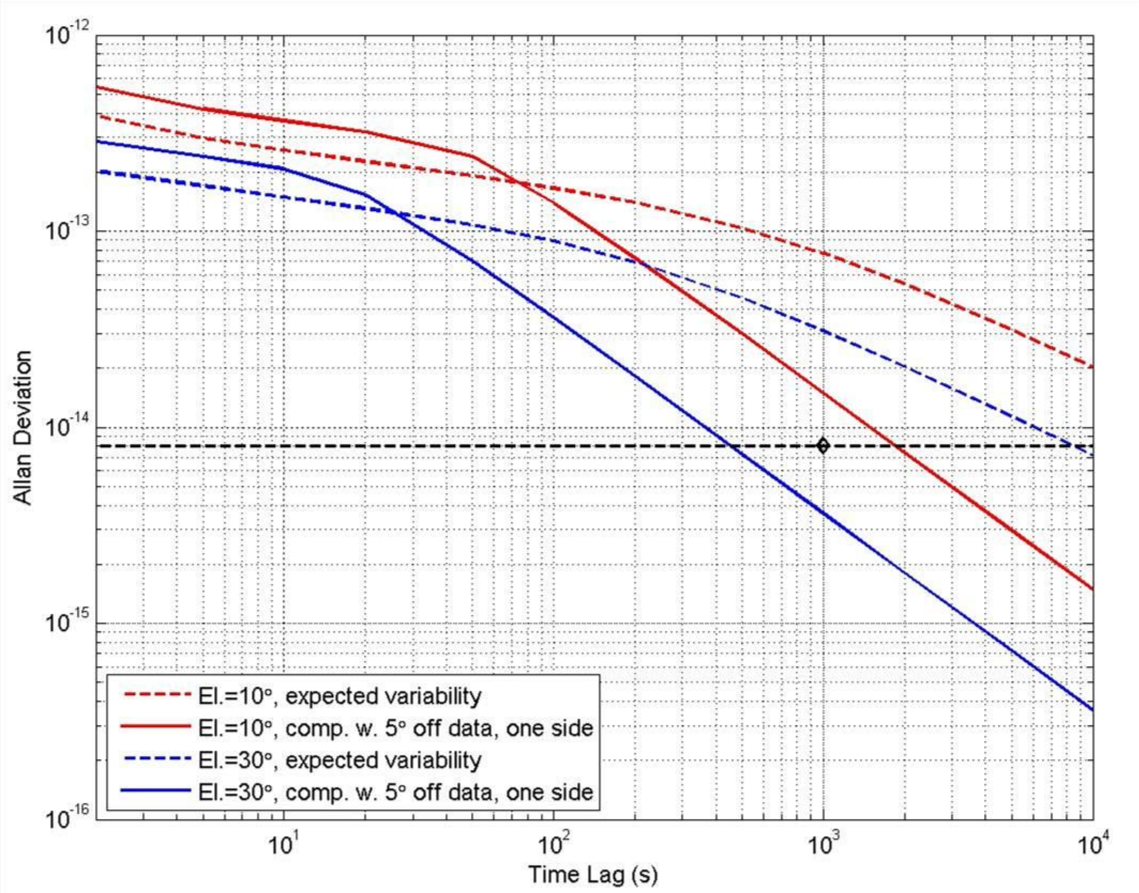

Figure 5.8: The Allan deviations due to the wet delay for elevation angles 10º and 30º (dashed lines) when using the model by Treuhaft and Lanyi and wind direction perpendicular to the observational directions. The solid lines show the remainder when the wet delay has been compensated using observations that are acquired 5º off the desired directions. At 1000 s the Allan deviation $8 \cdot 10^{-15}$, from the study's design criterion, has been marked.

Note that for short times "compensated" curves has greater ASD than the uncompensated. This is a result of the fact that variations along the line of sights separated by 5° are more or less uncorrelated for such short time spans. The data intended for compensation mainly introduce more noise on these small time lags.

Maximum pointing offsets related to the beam width of the radiometer are suggested in [AD. 8]. Based on this document the expected Allan deviations for pointing offsets 0.35°, 0.6°, and 1.8° were calculated. The resulting Allan deviations is presented in Figure 5.9.

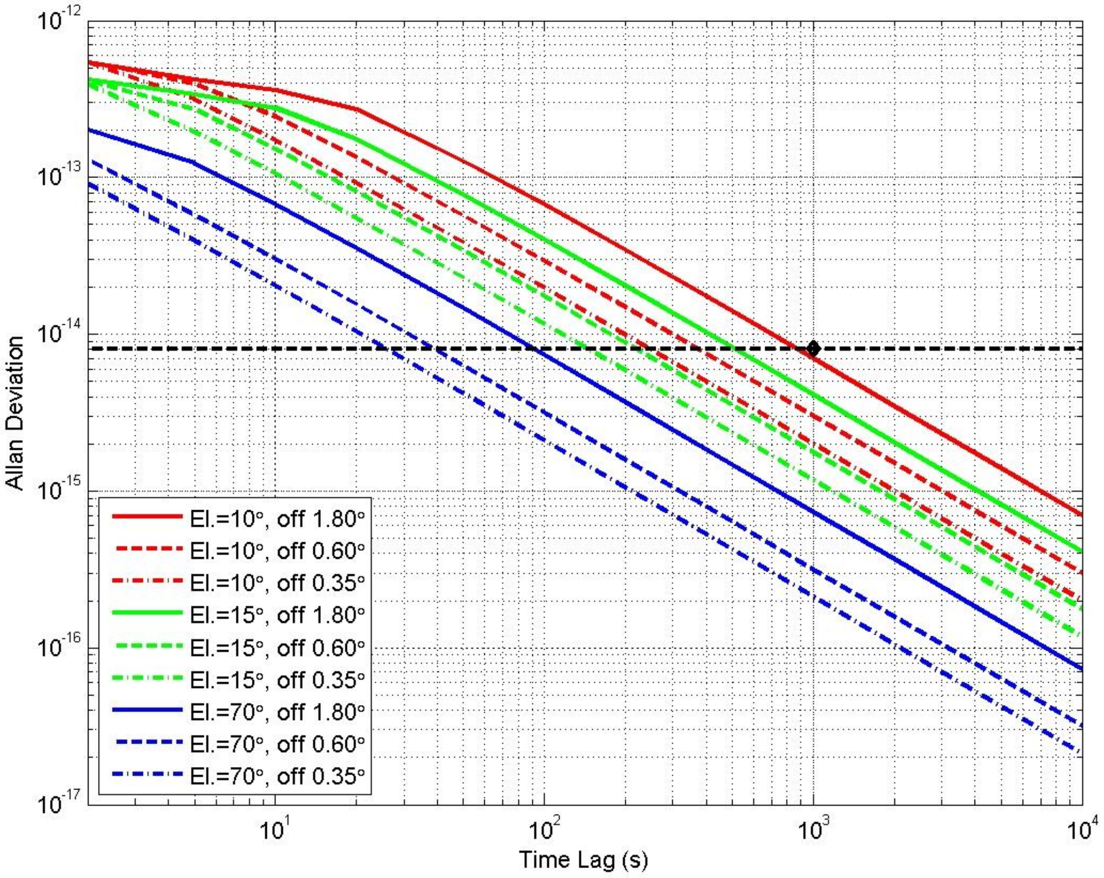

Figure 5.9: The Allan deviations due to the wet delay difference between a desired line of sight and lines with specific great circle distances off the desired line. The great circle distances investigated are 0.35º, 0.6º and 1.8º. The assumed elevation angles are 10º, 15º and 70º and the azimuth angle is 0º. The assumed wind direction is to the east. The study's design criteria, an Allan deviation of $8\cdot10^{-15}$ at 1000 s, is denoted by a diamond.

5.3.4 Optimal Combination of Data BLUE

Based on the structure function descriptions we can assess the possible benefit of using a combination of observations to calibrate the wet delay. We assume that we have *n* measurements; all scaled to the desired elevation angle, from which we form a linear combination, an estimator l_A of the desired wet delay l_D. By demanding that the sum of the weights equals one we get an unbiased estimator of the desired delay. We wish to find weights producing the Best Linear Unbiased Estimator (BLUE) in the sense that its error variance is minimal [RD. 33]. We can start by rewriting Equation (5-16) in matrix form. By defining the weight vector $w = \{w_1,\dots,w_n\}^T$ the structure function vector $D_D = \{E\{(l_1 - l_D)^2\},\dots,E\{(l_n - l_D)^2\}\}^T$ and similarly the matrix D_A with elements $D_{A;p,q} = E\{(l_p - l_q)^2\}$ we can write the equation

$$E\{(l_A - l_D)^2\} = w^T D_D - \tfrac{1}{2} \cdot w^T D_A w \qquad (5\text{-}19)$$

For completeness we also take into account the instrumental errors and add the resulting term $w^T C_I \ w$ based on the instrumental error covariance matrix C_I . A total error variance can then be written as

$$\varepsilon_w = w^T D_D - ½ \cdot w^T D_A w + w^T C_I w = w^T D_D - ½ \cdot w^T D_T w \tag{5-20}$$

where the last term originate from the combination $D_T = D_A - 2 \cdot C_I$.

The set of weights that minimizes ε_w, under the condition that the sum of the weights equals unity, is

$$w_{opt} = D_T^{-1} D_D + \frac{(1 - D_D^T D_T^{-1} s) \cdot D_T^{-1} s}{s^T D_T^{-1} s} \tag{5-21}$$

where s is a vector with ones, $s = \{1,\ldots,1\}^T$. Equation (5-21) is identical to one presented in [RD. 29] but here expressed using structure functions instead of covariance. The derivation is given in Annex A.3. The resulting minimum error variance is

$$\varepsilon_{opt} = ½ D_D^T D_T^{-1} D_D - ½ \frac{(1 - D_D^T D_T^{-1} s)^2}{s^T D_T^{-1} s} \tag{5-22}$$

Figure 5.7 can be seen as a simple illustration of the benefit of a linear combination, for the case of two measurements with an equal weight of 0.5 each.

5.4 Remote Sensing Techniques

In order to measure atmospheric turbulence we need observations with a high temporal resolution, or a high spatial resolution, or both of these. Turbulence is a rather wide concept. Depending on the application the focus can be on the variability of one or several atmospheric parameters, such as pressure, wind speed, wind direction, temperature, and humidity. In our application we deal with the impact on the propagation of radio waves and more specifically the variations in the propagation delay (an alternative expression is the excess propagation path) of radio signals in space-Earth paths. Therefore, measurements of the radio refractive index in the atmosphere are our main concern.

The radio refractive index is determined by the pressure, temperature, and humidity. As discussed earlier the structure constant C_n^2 is a derived parameter from measurements of the spatial or temporal variability of the refractivity and provides information on the strength of the turbulence.

The review of instruments that can be used to obtain information about atmospheric turbulence, and in particular the structure constant, is organized as follows. First we give examples of techniques using in situ measurements. Thereafter we discuss remote sensing techniques capable of estimating profiles of the structure constant. Finally, and also because the overall goal of this work is to correct received radio signals for the integrated effect, the focus will be on that type of instrumentation that measure and characterize the integrated effect along a specific observation path.

5.4.1 In Situ Measurements

5.4.1.1 Aircrafts

An obvious approach to get information about pressure, temperature, and humidity is to use an aircraft (A/C). High quality instruments with a high temporal resolution are needed. A good control of the spatial sampling is of course possible, although clear limitations exist if we want to acquire data along Earth-space paths with elevation angles larger than what is possible for the specific A/C. We assume that for most routine observations it is a too expensive method. A recent analysis using different instruments on two different aircrafts is given in [RD. 51]. They derive a relationship for estimating the structure constant of the wet component of the refractivity and apply the data to studies of the impact of turbulence on radio occultation observations. The aircraft's possible flight paths are favourable for these kinds of geometries.

5.4.1.2 Radiosondes

The classic method to obtain information about the atmosphere, and especially vertical profiles, is to launch radiosondes. Numerous publications describing and using radiosonde data exist. As a first assumption it seems that there should be vast amounts of radiosonde data available for studies of atmospheric turbulence. It is possible to estimate C_n^2 profiles from the normal radiosonde observations of pressure, temperature, humidity, and wind speed. Assuming that the small-scale fluctuations in the refractive index are created by turbulent mixing of large-scale refractive index variations, an expression for C_n^2 can be obtained. It is important to note that this method assumes cloud-free conditions, which can introduce significant uncertainties since it may be difficult to confirm this assumption when studying a specific radiosonde profile. In addition an assumption has to be made regarding the value of the outer scale of the turbulence.

Pioneering work, [RD. 75], used the method for comparisons with radar observations of turbulence. Although they used regular radiosonde data, with a vertical resolution limited to approximately 100 m, they pointed out that high resolution profiles would be more accurate and of course also determine the resolution of the C_n^2 profile.

In later work an intermittency factor was introduced in [RD. 17] which is used to describe that thin turbulent layers are often imbedded in large-scale laminar flows. These thin layers may not be detected at all if the vertical resolution of the radiosonde is of the order of a 100 m or more.

Examples of recent studies of atmospheric turbulence with high-resolution radiosondes are reported in [RD. 2] who analyzed 48 radiosonde ascents from the oceanic regions around India and the work [RD. 43] who used three years of daily radiosonde launches from the tropical station Gadanki (13.5°N, 79.2°E).

5.4.1.3 Thermosondes

A thermosonde is a special type of radiosonde which in addition to the measurements of pressure, temperature, humidity, also measures the variations in temperature over a horizontal distance (typically around 1 m) with high accuracy (typically of the order of 10^{-3} K). These measurements are used directly to estimate the temperature structure constant C_T^2 [RD. 10]. Therefore, thermosondes are often used to study turbulence effects on electromagnetic propagation in the optical range of the spectrum where the variations are mainly caused by temperature and variations in humidity are less important.

Unfortunately, similar horizontal gradient measurements of the humidity seem not to have been acquired. However, as described in [RD. 46], the temperature structure constant provides information on the product of the outer scale of the atmospheric turbulence and the so called intermittency factor, which improves the accuracy of the method using the high-resolution radiosonde data described above. A similar technique was used in [RD. 81] in order to carry out comparisons of the structure constant measured by a VHF radar (more details in the next section) and in situ measurements with thermosondes.

In a recent publication, [RD. 60], thermosondes are used and the results are compared to scintillation measurements in the near infrared (880 nm) over an 800 m long path and approximately 10 m above the ground. Among their conclusions are that there is an increase in the strength of the turbulence in the boundary layer during the day compared to the night due to different convective conditions.

5.4.2 Techniques with Profiling Possibilities

5.4.2.1 RADAR

Estimation of C_n^2 profiles can be carried out by using Doppler radar measurements. The power backscattered from a specific height is due to the irregularities caused by turbulence at that height. There exist a number of investigations where C_n^2 is measured with radars, although there are not many that investigate C_n^2 in the lower troposphere over longer time periods.

A study based on one year of data acquired in Colorado was reported in [RD. 75]. The C_n^2 profiles cover the range 5-15 km and the temporal resolution is 50 s. [RD. 15] presents data from an FM-CW Doppler radar using one year of observations at three different locations in Colorado, USA, with a 1 minute temporal resolution and a vertical resolution of approximately 0.5-1.5 km. [RD. 21] observe the so called Middle and Upper Atmosphere (MU). This is a VHF-band (46.5 MHz) Doppler radar where day and night observations are carried out in the 1-25 km range. *Rao* et al. [RD. 54] use the Indian Mesosphere-Stratosphere-Troposphere (MST) radar covering the height interval 4-20 km. Three days of observations from June 1994 are analyzed and compared to nearby results from radiosonde data. In Rao et al. [RD. 55] 3 years of data from the same station are analyzed, now for the height interval 7.5-21 km. Nastrom and Eaton [RD. 42] present 4 years of data from California using a VHF Doppler profiling radar providing data for the height interval 2-21 km. A more recent study [RD. 41] presents results from the years 2001-2004 from the same radar installation.

The radar systems that have been used to acquire information on atmospheric turbulence are unfortunately available only at a few locations worldwide. Another disadvantage is the difficulty to get information from the boundary layer, where most of the turbulence is found.

5.4.2.2 LIDAR

Atmospheric turbulence affects also electromagnetic waves in the optical part of the spectrum. In spite of the fact that the refractive index is different compared to the microwave region - where water vapour plays a more dominant role - optical propagation studies will give information on the dynamic atmosphere. Consequently, the radar concept in the optical region - referred to as LIDAR - has been used to study the cloud dynamics and the relationships to drop number concentration and drizzle formation [RD. 20].

An advantage with the lidar technique is that it can provide detailed observations from the boundary layer. This is e.g. demonstrated by *Kao* et al. [RD. 31] who produce maps with high resolution of the water vapour mixing ratio from the ground surface up to heights of several hundred metres with a spatial resolution of approximately 1.5 m.

5.4.2.3 SCIDAR

Atmospheric turbulence is a limiting effect for high resolution imaging using ground-based optical telescopes. A technique to measure the turbulence profile has been developed and is often referred to as SCIntillation Detection and Ranging (SCIDAR). One of the first descriptions was presented by Rocca et al. [RD. 61]. At that time it was, however, not possible to detect turbulent layers below a couple of kilometres. The technique has thereafter been improved. *Avila et* al. [RD. 9] reported on the so called generalized SCIDAR technique where turbulent layers can be detected already from the ground level. Soon after Avila et al. [RD. 8] reported on the first successful measurements of this type. More recently an example of using this technique together with adaptive optics for corrections of the telescope aperture has been described in the doctoral thesis by Egner [RD. 19].

5.4.3 Techniques Providing Integrated Observables

5.4.3.1 Radio Interferometry Methods

Radio interferometry was applied to radio astronomy already in the 1960ies, using both local arrays as well as global distances such as the VLBI technique. Using the Very Large Array (VLA) at 5 GHz *Armstrong and* Sramek [RD. 6] derived a spatial structure function based on the different baseline lengths. The power spectrum of the tropospheric phase fluctuations was in reasonable good agreement with those from water vapour radiometry observations.

A couple of years later *Resch* et al. [RD. 59] confirmed the VLA sensitivity to water vapour fluctuations by mounting two Water Vapour Radiometers (WVRs) in two VLA antennas. A similar experiment was later carried out, using a 22 km baseline at Goldstone in California, by *Linfield et* al. [RD. 38]. We will return to studies using WVRs for path delay estimations below. Additional studies of phase fluctuations aimed at monitoring the flow of water vapour across the VLA interferometer array have been reported by Jacobson and Sramek [RD. 27].

5.4.3.2 Satellite Link Measurements

The integrated effect of atmospheric turbulence is unavoidable and easily studied using satellite signals on the ground surface. A large amount of studies have been performed in order to acquire site dependent statistics. For example *Otung and* Evans [RD. 53] reported on measurements on the 20 GHz beacon signal from ESA's Olympus satellite. In a later paper Vasseur [RD. 76] used radiosonde data acquired during one year (1990) to compare scintillation statistics measured at a nearby site using beacon signals at 12.5 and 30 GHz from the same Olympus satellite. The sampling rate was 1 Hz. The agreement in terms the cumulative distributions of the variance of the scintillation over one year is excellent with a deviation less than 0.1 dB^2.

Additional examples of measurements and scintillation model development are published by Kassianides and Otung [RD. 32] (model for simulating the performance of scintillation-degraded communication links), Otung and Savvaris [RD. 52] (formulas to improve the estimation of tropospheric scintillation), and *Singh et* al. [RD. 66] (scintillation statistics acquired at 10 GHz in Malaysia).

5.4.3.3 Scintillation and Path Delay Along the Ground

Scintillation measurements along paths on the ground have been performed for many years. For example, *Herbstreit and* Thompson [RD. 24] reported on measurements at 172.8 and 1046 MHz along paths from 3.5 to 60 miles in Colorado, USA. More recently Lüdi and Magun [RD. 39] used mm-waves along a line-of-sight path, on the average 200 m above the ground, in Bern, Switzerland, to derive values for the refractivity structure constant. The system was also used in El Leoncito, Argentina, in desert-like conditions, where the structure constant values were approximately ten times smaller.

The interesting concept to carry out simultaneous path delay measurements at optical and at radio frequencies was described by Thompson [RD. 72]. A similar system was developed about twenty years later, with the goal to measure along Earth-space paths, using an aircraft. To our knowledge also this system has so far only been used along ground paths as described by Walter and Bender [RD. 77].

5.4.3.4 GNSS

The idea to use Global Navigational Satellite Systems (GNSS) for turbulence studies is a special case of a satellite link monitoring system. An interesting advantage is that the transmitted phase of the GNSS signals is already used in applications for precise position estimates. We may also regard the method as a special case (but slightly different) of interferometry using radio astronomy telescopes. Since GNSS signals are much stronger than are the signals from the radio astronomy sources the antennas needed are significantly smaller and hence also inexpensive (in relative terms).

A huge number of papers has been written concerning the possibility to estimate atmospheric effects and then especially the amount of water vapour. An interesting application, e.g., for weather services is to have such estimates in close to real time for usage in weather forecasting. However, in this case compromises have to be made in terms of accuracy. Here we focus on the work motivated by studies of atmospheric turbulence. Such studies have been carried out by Schön and Brunner [RD. 65] reporting on the correlations of GPS carrier-phase observations and their dependence on the separation distance between the two receivers. Using such information Schön and Brunner [RD. 64] have consequently proposed improved modelling of atmospheric effects when processing GPS data, and especially in small GPS networks.

Also Nilsson et al. [RD. 47] have shown that a very dense ground-based network of GPS receivers has the possibility to study and estimate several relevant parameters in atmospheric turbulence models. These parameters can thereafter be used to, at least statistically, characterize the turbulence in that specific area.

More recently Nilsson and Haas [RD. 46] used single GPS receivers at participating sites in the so called CONT08 geodetic VLBI experiment to characterize the (size of) turbulence. These statistical parameters were then used to simulate atmospheric delays which in turn were included in simulated VLBI observations which in many aspects were consistent with the observed inaccuracies of the estimated coordinates from the real VLBI observations.

5.4.3.5 Solar Spectroscopy

Another remote sensing method is to use a background source (outside the atmosphere) and study the varying atmospheric absorption at selected frequencies in the optical/infrared part of the spectrum observed from the ground. There are many different applications of solar spectroscopy. Of relevance to this study is, e.g., the work by Somieski et al. [RD. 67] where a spectrometer (728-915 nm) is used to measure the atmospheric water vapour content along the line of sight towards the sun. We note that this application may be of specific interest also for this study as a possible validation technique. It is, however, important to note that clear skies are required.

5.4.3.6 Microwave Radiometry

Since this whole study is focused on developing microwave radiometry for correction of propagation delays in Earth-space paths, and especially over short time scales, we chose here to just give a couple of relevant examples of papers published. The Jet Propulsion Laboratory (JPL) in California has been very active in the area. The use of WVRs at the VLA by *Resch et al.* [RD. 59] was already mentioned above. Later development at JPL has resulted in WVRs with extremely high stability. These have been described by *Tanner* [RD. 69] and *Tanner and* Riley [RD. 70].

Although one possible resulting parameter from WVR observations is the excess propagation delay caused by water vapour, we may still want to estimate a structure-constant profile, but then the shape of the profile has to be assumed. For example, *Treuhaft and Lanyi* [RD. 74] made the simple assumption that C_n^2 was constant up to an effective tropospheric height and zero above. *Nilsson et al*. [RD. 48] estimated C_n^2 from variations between slant wet delays measured in different directions by a ground based microwave radiometer. Also in this case, assumptions about the shape of the profile must be made.

We also like to mention the application of radiometric measurements in combination with radio interferometer arrays. *Carilli and Holdaway* [RD. 14] discuss the needed sensitivity of the radiometers at different frequencies. It may be relevant to note, that for very dry sites it may be favourable to use radiometry at the water vapour line at 183 GHz. On the other hand, at very dry sites the variability is also expected to be significantly smaller.

Finally, it may be of interest to note that although the standard radiometer for path length corrections uses two or more frequencies, it is an advantage in terms of noise to use only one frequency channel during clear sky conditions. Jarlemark and Elgered [RD. 28] showed the concept of a one-channel radiometer using the temporal variability to draw conclusions concerning the delay quality.

6 INTERFACES AND OPERATIONAL ISSUES RELEVANT TO MICROWAVE RADIOMETER

The only example of use of microwave radiometry to estimate the troposphere path delay in the context of Deep Space tracking is represented by the AMC systems developed in support of the Cassini cruise radio science experiments [RD. 70]. Apart from the excellent performance obtained by the AMC in reducing tropospheric noise on Cassini's Doppler observables path delay [RD. 5] [RD. 73] [RD. 11] a number of operational issues were noticed during routine operations of the radiometers since 2001.

The most serious concern is relative to the time synchronization of the AMC, which could reflect in a potentially bad time-tagging of the brightness temperature readings, acquired by the microwave radiometer instrument, within the AMC. In particular, the time reference of the AMC systems is given by the quartz internal to the embedded Personal Computer used to control locally the AMC. If, for any reason, the internal time-update process, handled by the on-board operating system, fails to happen for a long time span, the large drifts of the quartz clock may cause de-synchronizations of the AMC internal time as large as tens of seconds in a few weeks. This time-tagging error may represent a relatively large error contribution in the performance of the AMC in reducing tropospheric noise, as the intrinsically high frequency fluctuations of the wet part of the Earth troposphere are not correctly time-referenced.

A second issue is represented by the large physical distance between the actual unit (mounted at the ground station site) and its operator. Planned maintenance and check-out controls of the unit must necessarily be enabled using remote operations, so that hands-on operations should be limited to periodic inspections or to extraordinary maintenance.

In addition, there is the need to archive all media calibration data at both sites (ground station and operation center), so that at least one is independent of long communication lines (typically the internet is used). In order to correct the above issues and to implement the said archiving requirements, the following preliminary block diagram can be proposed, Figure 6.1.

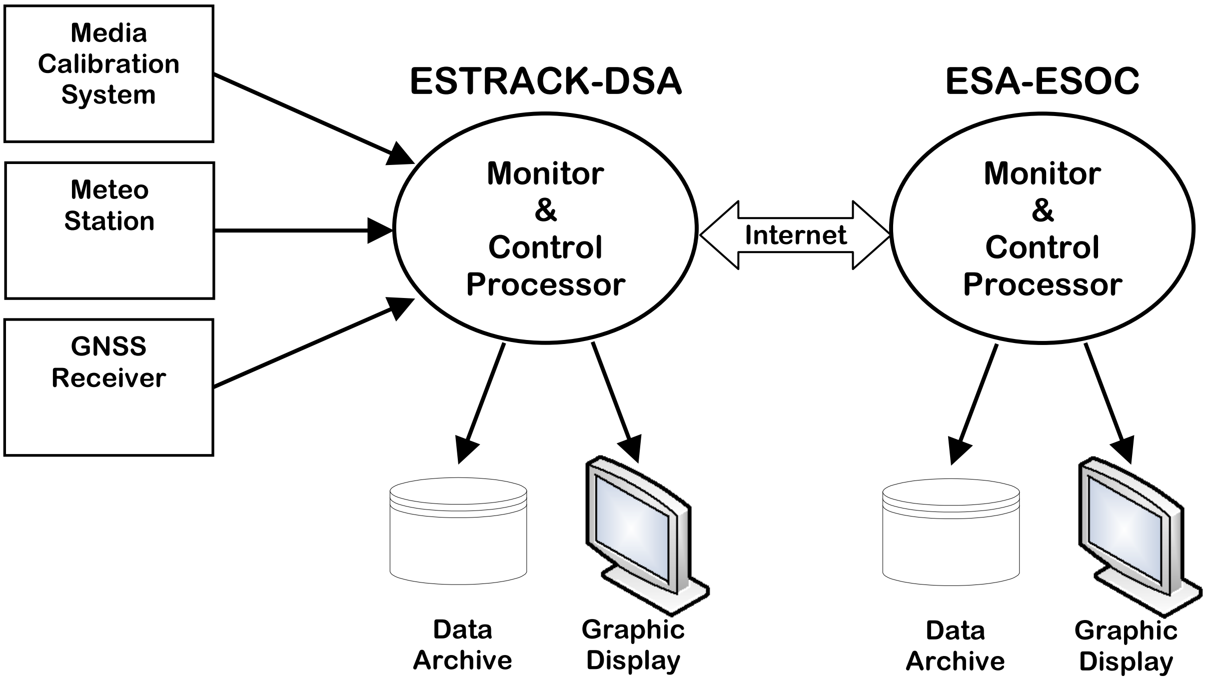

Figure 6.1: Block diagram of the high-level connections of the Media Calibration System

In order to detail the design of the interfaces between the instrument on the left of Figure 6.1 to the local Monitor & Control Processor, it is worth keeping into account the following functional requirements:

- Receive Instrument Output Data
    - Download data from MCS, meteo station and GNSS receiver
    - Format records of measured data set
- Provide Instrument Control Data
    - Provide time synchronization of instruments with ESTRACK
    - Provide MCS antenna tracking data (azimuth, elevation, vs. time)
- Provide Data to Radio Science investigators
    - Path delay time series
    - Provide path delay data quality flags
    - Compute internal consistency of path delay retrievals
    - Provide real time instrument malfunction warnings
- Archive data
    - Archive Media Calibration raw and processed data

A possible implementation satisfying the requirements above is shown in Figure 6.2

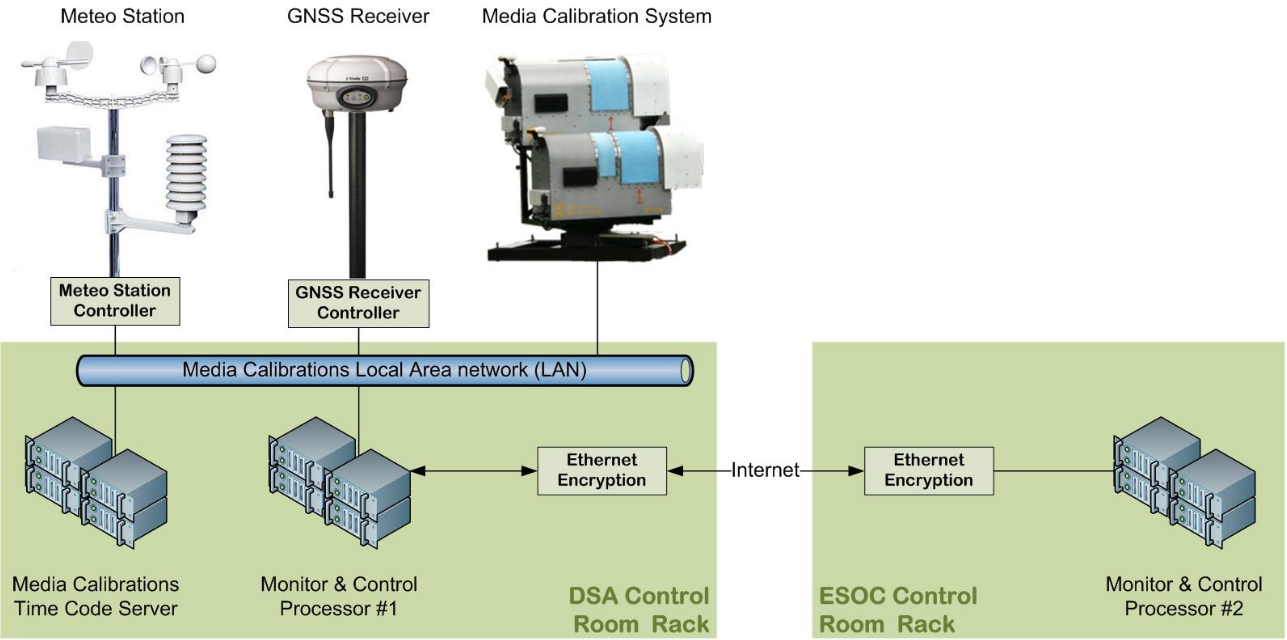

Figure 6.2: Block diagram of the low-level connections of the media calibration instrumentation

Apart from being a possible backup for the microwave radiometer system to estimate the tropospheric path delay, the GNSS receiver provides a precise time reference, to be elaborated by the Time Code Server and distributed over the Media Calibrations LAN (locally) and, via the internet, to the ESOC-based Control Room Rack. The connection between the (external) instrumentation and the (internal) LAN may be realized through Ethernet cables or, if deemed more reliable, through fiber optic cables (in this case, dedicated controllers are required within the rack to convert optical signals to the LAN standard.

7 ANNEXES

A.1 Variance of Wet Delay Differences in Different Directions

The slant atmospheric delay along a path A can be parameterized as:

$$l_{A,0} = \int [n(\vec{r}_A(s_A)) - 1] ds_A = \frac{1}{\sin\theta_A} \int [n(\vec{r}_A(v)) - 1] dv$$

using the relation $\sin\theta_A \cdot ds_A = dv$ between the slant and vertical differentials. Disregarding the curvature of the earth we can assume that

$$E\left\{\int [n(\vec{r}_A(v)) - 1] dv\right\} = E\left\{\int [n(\vec{r}_B(v)) - 1] dv\right\}$$

for two paths A and B with fairly similar elevation angles. We can therefore use the sine function to scale one slant wet delay to its equivalent value at another elevation angle. The original slant delay $l_{A,0}$ scaled to the desired elevation angle θ_{ref} is then

$$l_A = \frac{\sin\theta_A}{\sin\theta_{ref}} \cdot l_{A,0} = \frac{1}{\sin\theta_{ref}} \int [n(\vec{r}_A(v)) - 1] dv$$

We form the square of scaled wet delay difference as

$$(l_A - l_B)^2 = (l_A - l_B) \cdot (l_A - l_B) = \frac{1}{\sin\theta_{ref}} \int [n(\vec{r}_A(v)) - n(\vec{r}_B(v))] dv \cdot \frac{1}{\sin\theta_{ref}} \int [n(\vec{r}_A(v')) - n(\vec{r}_B(v'))] dv' =$$

$$\frac{1}{\sin^2\theta_{ref}} \iint [n(\vec{r}_A(v)) - n(\vec{r}_B(v))] \cdot [n(\vec{r}_A(v')) - n(\vec{r}_B(v'))] dv dv' =$$

$$\frac{1}{2\sin^2\theta_{ref}} \iint \Big[[n(\vec{r}_A(v)) - n(\vec{r}_B(v'))]^2 + [n(\vec{r}_B(v)) - n(\vec{r}_A(v'))]^2 -$$

$$[n(\vec{r}_A(v)) - n(\vec{r}_A(v'))]^2 - [n(\vec{r}_B(v)) - n(\vec{r}_B(v'))]^2 \Big] dv dv' =$$

$$\frac{1}{2\sin^2\theta_{ref}} \cdot \iint \Big[2 \cdot [n(\vec{r}_A(v)) - n(\vec{r}_B(v'))]^2 - [n(\vec{r}_A(v)) - n(\vec{r}_A(v'))]^2 - [n(\vec{r}_B(v)) - n(\vec{r}_B(v'))]^2 \Big] dv dv'$$

where we have formed squares using

$$(a-b) \cdot (c-d) = \tfrac{1}{2}[(a-d)^2 + (b-c)^2 - (a-c)^2 - (b-d)^2]$$

By interchanging the order between expectation value and integration, $E\left\{\iint dv dv'\right\} = \iint E\{\ \} dv dv'$, we now get the sought variance from the definition of refractivity structure function:

$$E\{(l_A - l_B)^2\} = \frac{1}{2\sin^2\theta_{ref}} \cdot \iint [2 \cdot D_{n(R)}(|\vec{r}_A(v) - \vec{r}_B(v')|) - D_{n(R)}(|(\vec{r}_A(v) - \vec{r}_A(v')|) - D_{n(R)}(|(\vec{r}_B(v) - \vec{r}_B(v')|)]dvdv'$$

A.2 Structure Function of a Linear Combination

Consider a desired atmospheric delay, l_D, and an alternative, l_A, which is a sum of delays:

$$l_A = \sum w_p \cdot l_p$$

where $\sum w_p = 1$.

To evaluate the variance of the difference, $E\{(l_A - l_D)^2\}$ we start by expressing the difference as:

$$l_A - l_D = \sum_p w_p (l_p - l_D)$$

We use the algebraic relation $(a-c)\cdot(b-c) = ½\cdot[(a-c)^2 + (b-c)^2 - (a-b)^2]$ in order to express products as squares. The sought squared difference can then be written as:

$$\begin{aligned}
&(l_A - l_D)^2 = \sum_p \sum_q w_p w_q \cdot (l_p - l_D)\cdot(l_q - l_D) = \\
&½ \cdot \sum_p \sum_q w_p w_q \cdot [(l_p - l_D)^2 + (l_q - l_D)^2 - (l_p - l_q)^2] = \\
&½ \cdot \sum_p \sum_q w_p w_q \cdot [(l_p - l_D)^2 + (l_q - l_D)^2] - ½ \cdot \sum_p \sum_q w_p w_q \cdot (l_p - l_q)^2 = \\
&½ \cdot \sum_p w_p \cdot [(l_p - l_D)^2 + (l_p - l_D)^2] \cdot \sum_q w_q - ½ \cdot \sum_p \sum_q w_p w_q \cdot (l_p - l_q)^2 = \\
&\sum_p w_p \cdot (l_p - l_D)^2 - ½ \cdot \sum_p \sum_q w_p w_q \cdot (l_p - l_q)^2
\end{aligned}$$

Consequently:

$$\begin{aligned}
&E\{(l_A - l_D)^2\} = \\
&\sum_p w_p \cdot E\{(l_p - l_D)^2\} - ½ \cdot \sum_p \sum_q w_p w_q \cdot E\{(l_p - l_q)^2\}
\end{aligned}$$

A.3 BLUE Derivation

Based on the structure function descriptions we can assess the possible benefit of using a combination of observations. Following Kay [RD. 33] we first add a term $\lambda \cdot (w^T s - 1)$ to the error variance ε_w. For the sought case of $w^T s = 1$ this extra term is zero. We get:

$$\varepsilon_L = \varepsilon_w + \lambda \cdot (w^T s - 1) = w^T D_D - ½ \cdot w^T D_T w + \lambda \cdot (w^T s - 1)$$

Find the gradient and set it to zero:

$$\frac{\partial \varepsilon_L}{\partial w} = D_D - D_T w + \lambda \cdot s = \vec{0}$$

and identify the optimum w at zero gradient:

$$w_{opt} = D_T^{-1} D_D + \lambda \cdot D_T^{-1} s$$

We then find λ for which the sum of the weights is unity:

$$w_{opt}^T s = D_D^T D_T^{-1} s + \lambda_u \cdot s^T D_T^{-1} s = 1 \Rightarrow$$

$$\lambda_u = \frac{1 - D_D^T D_T^{-1} s}{s^T D_T^{-1} s}$$

Applying λ_u in the equation for optimal weights w_{opt} give the sought equation:

$$w_{opt} = D_T^{-1} D_D + \frac{(1 - D_D^T D_T^{-1} s) \cdot D_T^{-1} s}{s^T D_T^{-1} s}$$